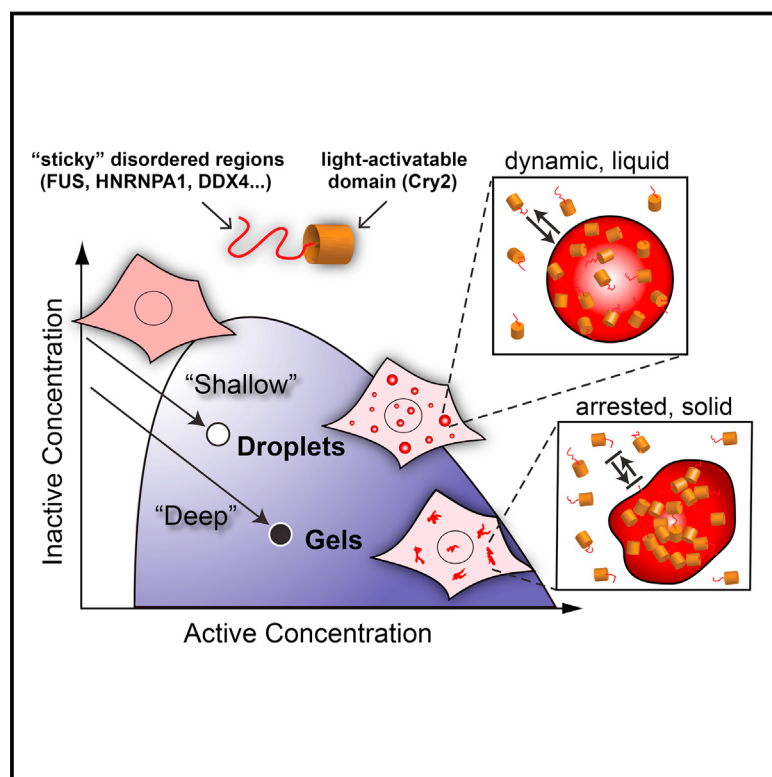


Spatiotemporal Control of Intracellular Phase Transitions Using Light-Activated optoDroplets

Graphical Abstract



Authors

Yongdae Shin, Joel Berry,
Nicole Pannucci, Mikko P. Haataja,
Jared E. Toettcher,
Clifford P. Brangwynne

Correspondence

toettcher@princeton.edu (J.E.T.),
cbrangwy@princeton.edu (C.P.B.)

In Brief

Light-dependent triggering of protein association allows selective temporal and spatial control of droplet and gel formation aimed at understanding the different forms of membrane-less bodies and fibrillar structures within cells.

Highlights

- OptoDroplets enable light-activatable control of intracellular phase transitions
- Rapid growth and fast inactivation lead to droplet assembly in subcellular regions
- Cells driven to deep supersaturation form solid-like gels
- Gels are initially reversible but undergo aging into irreversible aggregates

Spatiotemporal Control of Intracellular Phase Transitions Using Light-Activated optoDroplets

Yongdae Shin,¹ Joel Berry,² Nicole Pannucci,³ Mikko P. Haataja,² Jared E. Toettcher,^{3,*} and Clifford P. Brangwynne^{1,4,*}

¹Department of Chemical and Biological Engineering, Princeton University, Princeton, NJ 08544, USA

²Department of Mechanical and Aerospace Engineering, Princeton University, Princeton, NJ 08544, USA

³Department of Molecular Biology, Princeton University, Princeton, NJ 08544, USA

⁴Lead Contact

*Correspondence: toettcher@princeton.edu (J.E.T.), cbrangwy@princeton.edu (C.P.B.)

<http://dx.doi.org/10.1016/j.cell.2016.11.054>

SUMMARY

Phase transitions driven by intrinsically disordered protein regions (IDRs) have emerged as a ubiquitous mechanism for assembling liquid-like RNA/protein (RNP) bodies and other membrane-less organelles. However, a lack of tools to control intracellular phase transitions limits our ability to understand their role in cell physiology and disease. Here, we introduce an optogenetic platform that uses light to activate IDR-mediated phase transitions in living cells. We use this “optoDroplet” system to study condensed phases driven by the IDRs of various RNP body proteins, including FUS, DDX4, and HNRNPA1. Above a concentration threshold, these constructs undergo light-activated phase separation, forming spatiotemporally definable liquid optoDroplets. FUS optoDroplet assembly is fully reversible even after multiple activation cycles. However, cells driven deep within the phase boundary form solid-like gels that undergo aging into irreversible aggregates. This system can thus elucidate not only physiological phase transitions but also their link to pathological aggregates.

INTRODUCTION

Cellular function relies on coordinating the thousands of reactions that simultaneously take place within the cell. Cells accomplish this task, in large part, by spatio-temporally controlling these reactions using diverse intracellular organelles. In addition to classic membrane-bound organelles such as secretory vesicles, mitochondria, and the endoplasmic reticulum, cells harbor a variety of membrane-less organelles. Most of these are abundant in both RNA and protein and are referred to as ribonucleoprotein (RNP) bodies. Among dozens of examples are nuclear bodies such as nucleoli, Cajal bodies, and PML bodies, and cytoplasmic germ granules, stress granules, and processing bodies (Mao et al., 2011; Anderson and Kedersha, 2009; Buchan and Parker, 2009; Handwerger and Gall, 2006). By impacting a number of RNA processing reactions within cells, these structures appear to play a central role in controlling the

overall flow of genetic information and are also increasingly implicated as crucibles for protein aggregation pathologies (Li et al., 2013; Ramaswami et al., 2013).

From a biophysical standpoint, these structures are remarkable in that they have no enclosing membrane and yet their overall size and shape may be stable over long periods (hours or longer), even while their constituent molecules exhibit dynamic exchange over timescales of tens of seconds (Phair and Misteli, 2000). Moreover, many of these structures have recently been shown to exhibit additional behaviors typical of condensed liquid phases. For example, P granules, nucleoli, and a number of other membrane-less bodies will fuse into a single larger sphere when brought into contact with one another (Brangwynne et al., 2009, 2011; Feric and Brangwynne, 2013) in addition to wetting surfaces and dripping in response to shear stresses. These observations have led to the hypothesis that membrane-less organelles represent condensed liquid states of RNA and protein that assemble through intracellular phase separation, analogous to the phase transitions of purified proteins long observed in vitro by structural biologists (Ishimoto and Tanaka, 1977; Vekilov, 2010). Consistent with this view, RNP bodies and other membrane-less organelles appear to form in a concentration-dependent manner, as expected for liquid-liquid phase separation (Brangwynne et al., 2009; Weber and Brangwynne, 2015; Nott et al., 2015; Wippich et al., 2013; Mollie et al., 2015). These studies suggest that cells can regulate membrane-less organelle formation by altering proximity to a phase boundary. Movement through such an intracellular phase diagram could be accomplished by tuning concentration or intermolecular affinity, using mechanisms such as posttranslational modification (PTM) and nucleocytoplastic shuttling.

Recent work has begun to elucidate the molecular driving forces and biophysical nature of intracellular phases. Weak multivalent interactions between molecules containing tandem repeat protein domains appear to play a central role (Li et al., 2012; Banjade and Rosen, 2014). A related driving force is the promiscuous interactions (e.g., electrostatic, dipole-dipole) between segments of conformationally heterogeneous proteins, known as intrinsically disordered protein/regions (IDP/IDR), which are typically low complexity sequences [LCS]. RNA binding proteins often contain IDRs with the sequence composition biased toward amino acids including R, G, S, and Y, which comprise sequences that have been shown to be necessary and sufficient for driving condensation into liquid-like protein

droplets (Elbaum-Garfinkle et al., 2015; Nott et al., 2015; Lin et al., 2015). The properties of such *in vitro* droplets have recently been found to be malleable and time-dependent (Elbaum-Garfinkle et al., 2015; Zhang et al., 2015; Weber and Brangwynne, 2012; Mollieix et al., 2015; Lin et al., 2015; Xiang et al., 2015; Patel et al., 2015), underscoring the role of IDR/LCSs in both liquid-like physiological assemblies and pathological protein aggregates.

Despite these advances, almost all recent studies rely primarily on *in vitro* reconstitution, due to a lack of tools for probing protein phase behavior within the living cellular context. However, a growing suite of optogenetic tools has been developed to control protein interactions in living cells. The field has primarily focused on precise control over homo- or hetero-dimerization (Toettcher et al., 2011; Kennedy et al., 2010; Levskaya et al., 2009), although recent work suggests the potential of optogenetics for studying intracellular phases; light-induced protein clustering can be used to activate cell surface receptors (Bugaj et al., 2013), as well as to trap proteins into inactive complexes (Lee et al., 2014; Taslimi et al., 2014).

Here, we introduce an optogenetic platform that can be used to dynamically modulate intracellular protein interactions, enabling the spatiotemporal control of phase transitions within living cells. We demonstrate the ability to induce reversible liquid-liquid phase separation, both globally and at specific subcellular locations. This system reveals that the location within the phase diagram dictates the material state of phase-separated IDR clusters—ranging from dynamic liquid droplets to arrested but reversible gels, which can over time mature into irreversible aggregates.

RESULTS

Fusing Intrinsically Disordered Proteins to Cry2 Leads to Rapid Light-Dependent Clustering

Many RNA binding proteins contain self-associating IDRs that can drive phase separation (Nott et al., 2015; Elbaum-Garfinkle et al., 2015; Lin et al., 2015; Patel et al., 2015; Mollieix et al., 2015). However, additional RNA binding domains can enhance phase separation via multivalent interactions with RNA. For example, FUS is an ALS-related RNA binding protein involved in diverse nucleic acid processing including DNA repair, transcription and pre-mRNA splicing (Schwartz et al., 2015; Dornmann and Haass, 2013). While the self-associating N-terminal IDR of FUS has been shown to be necessary and sufficient for liquid-liquid phase separation (Patel et al., 2015), C-terminal RNA binding domains appear to further promote phase separation (Burke et al., 2015; Lin et al., 2015).

Inspired by these prior *in vitro* findings, we sought to dynamically tune the interaction strength within living cells and thereby control intracellular phase transitions. To accomplish this, we fused the “sticky” IDR from various proteins to the photolyase homology region (PHR) of *Arabidopsis thaliana* Cry2, a light-sensitive protein which is known to self-associate upon blue light exposure (Bugaj et al., 2013) (Figure 1A). We reasoned that an IDR-Cry2 fusion protein would recapitulate the modular domain architecture of many phase separating proteins, but confer tunable light-dependence to its multivalent interactions.

We first expressed mCherry-labeled Cry2 PHR (Cry2WT) in NIH 3T3 cells and tested blue light-mediated clustering. Consistent with previous reports (Taslimi et al., 2014; Lee et al., 2014), Cry2WT alone showed little clustering upon blue light activation (Figure 1B). Strikingly, fusing the N-terminal IDR of FUS (FUS_N) to Cry2WT (optoFUS) leads to rapid blue light-dependent cluster assembly in most cells (Figures 1B and 1C). We find similar results upon fusing the C-terminal IDR of the ALS-related RNA binding protein HNRNPA1 (optoHNRNPA1), or the N-terminal IDR of DDX4 (optoDDX4), both of which have been reported to drive liquid-liquid phase separation (Nott et al., 2015; Mollieix et al., 2015) (Figures 1B and 1C).

optoDroplet Formation Exhibits a Threshold in Both Concentration and Light Intensity

The rapid light-activated assembly of our optoIDR constructs into spherical, droplet-like clusters suggests this assembly process may represent light-inducible phase separation within the cell. Consistent with this hypothesis, we frequently observe small clusters dissolving at the expense of larger nearby droplets, particularly within the nucleus (Figure S1A). This is reminiscent of an effect known as Ostwald ripening, well known to occur in systems undergoing phase separation (Voorhees, 1992).

We speculated that intracellular phase separation could arise from an increased self-association affinity of Cry2 upon blue light activation, which would represent a controllable change to the effective valency of the constructs, resulting in the crossing of a phase boundary above a saturation concentration. To test this picture, we took advantage of the ability to change the concentration of light-activated constructs using two independent methods: (1) by changing blue light intensity, and (2) by changing the total concentration of optoIDR molecules within the cell. Consistent with light-activated phase separation, the formation of optoFUS droplets shows a strong dependence on blue light activation intensity (Figure 2A; Movie S1). For an activation protocol that begins at a very weak power, we initially find that no cells exhibit droplets, even after continuous weak blue light activation for 16 min. However, when we tripled the blue light power, those cells that express high levels of the optoFUS construct assemble droplets. Distinct and spatially separated droplets slowly nucleate and then grow in size; similar behavior is seen in both optoDDX4 and optoHNRNPA1 constructs (Figures S1B and S1C). Qualitatively, this behavior is very similar to the well-known nucleation and growth regime observed in phase separating systems that are only shallowly supersaturated (Vekilov, 2010). Upon increasing blue light power further, even cells with low-expression of optoFUS rapidly assemble droplets, highlighting the switch-like behavior of light-induced clustering.

We next tested the dependence of droplet assembly kinetics on the total concentration of optoFUS. Blue light power was fixed and assembly was examined in cells with different expression levels (Figure 2B); we estimated intracellular optoFUS concentrations ranging from 0.2–13 μM (see the STAR Methods), comparable to the estimated intracellular concentration of endogenous FUS (~1–10 μM) (Patel et al., 2015). Consistent with the results obtained for varying blue-light activation, we observe that the lowest expressing cells do not form droplets at all. Interestingly, for cells that do form droplets, the higher

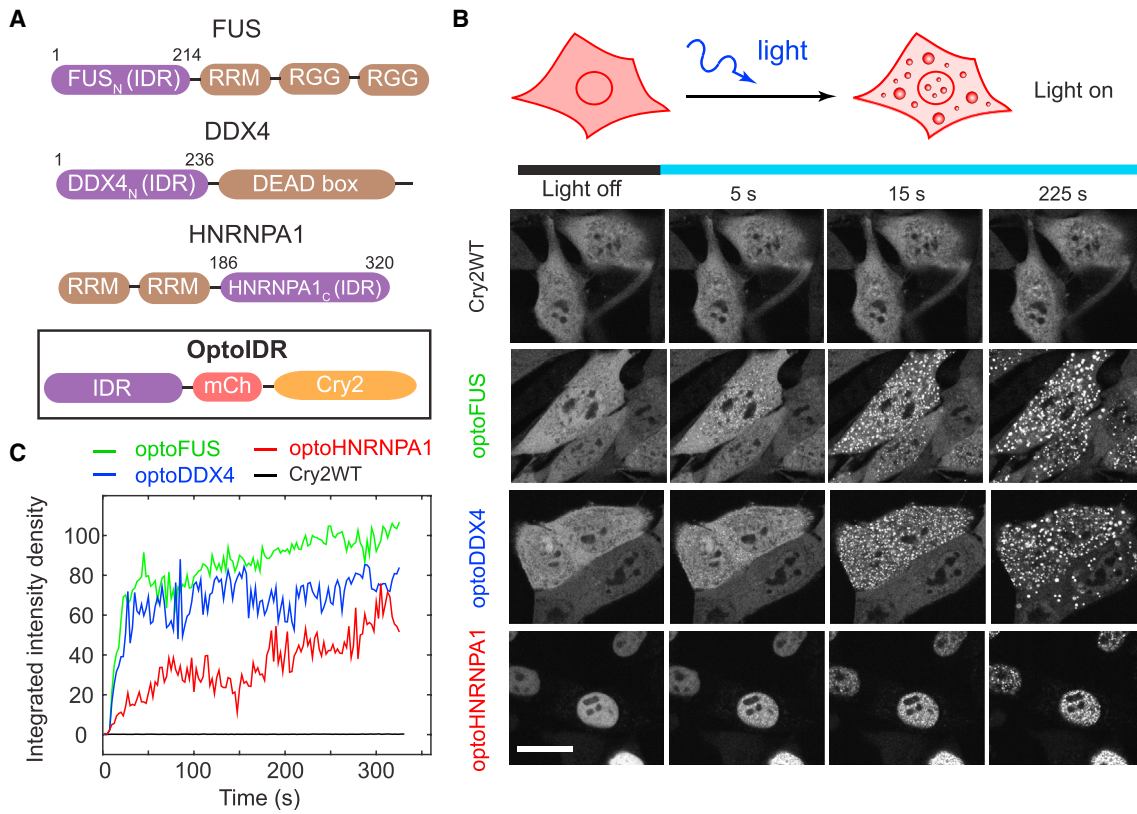


Figure 1. Rapid Light-Dependent Clustering of IDR Fused Cry2

(A) Schematic diagram of the optogenetic platform. Three IDR-containing RNA binding proteins are used in this study: FUS, DDX4, and HNRNPA1. The “optoIDR” construct consists of the N-terminal IDR fused to mCherry fluorescent protein and the Cry2PHR domain.

(B) Blue light activation of optoIDRs leads to rapid clustering in living cells. Representative fluorescence images of light-activated assembly of Cry2WT, optoFUS, optoDDX4, and optoHNRNPA1. All cells here are at similar expression levels and activated under identical conditions. Scale bar, 20 μ m.

(C) Temporal evolutions of integrated fluorescence intensity density of cytoplasmic (except optoHNRNPA1 that predominantly localized in nucleus) clusters for cells shown in (B).

the expression level, the faster the assembly kinetics (Figure 2B); similar behavior was seen with optoDDX4 and optoHNRNPA1 (Figures S1D and S1E). Moreover, higher expressing cells exposed to weaker blue light show similar clustering kinetics as lower expressing cells exposed to stronger light (Figure 2C). Taken together, these data suggest that the concentration of light-activated optoIDR is a key determinant for droplet formation.

A Kinetic Model of Light-Induced Phase Separation Quantitatively Matches Experimental Observations

To quantitatively test whether this system reflects light-controllable phase separation, we developed a simple kinetic framework for measuring the concentration of activated molecules and its relationship to the onset of droplet condensation. We assume that the inactivated state undergoes a first-order reaction to the activated state, with a reaction rate proportional to light intensity, according to $k_1 = k_{act} * [blue]$, where k_{act} is an activation rate constant and $[blue]$ is the intensity of activating blue light (Figure 3A). The activated molecules can also convert back to the inactivated state, at a rate given by k_2 . In this model, blue light

exposure increases the concentration of activated, self-associating molecules, which drives global phase separation upon exceeding the saturation concentration, i.e., when $C_{act} > C_{sat}$.

To test our phase separation model, we employed a series of activation protocols with different activation intervals and blue light power (Figures 3B and S2A). We utilize cycles of light followed by dark, because this allows us to probe both the activation rate constant, k_{act} , and the inactivation rate constant, k_2 . When optoFUS cells are exposed to a pulse train of activating light stimuli with high enough intensity, cells form droplets typically after a short lag phase. As molecules are recruited into droplets, the background concentration (fluorescence intensity) outside of droplets decreases (Figures S2B and S2C). When the interval between consecutive pulses is long, we observe cycles of partial assembly and disassembly, but for intervals shorter than 1 min the background intensity exhibits a monotonic decay to a steady state, $C_{bg,st}$ (Figures S2B and S2C).

In the simplest phase-transition model, the steady-state background concentration is equal to a sum of the concentration of inactivated molecules, $C_{inact,st}$, and the activated molecules outside clusters, C_{sat} (Figure 3B). Expressing $C_{inact,st}$ as a

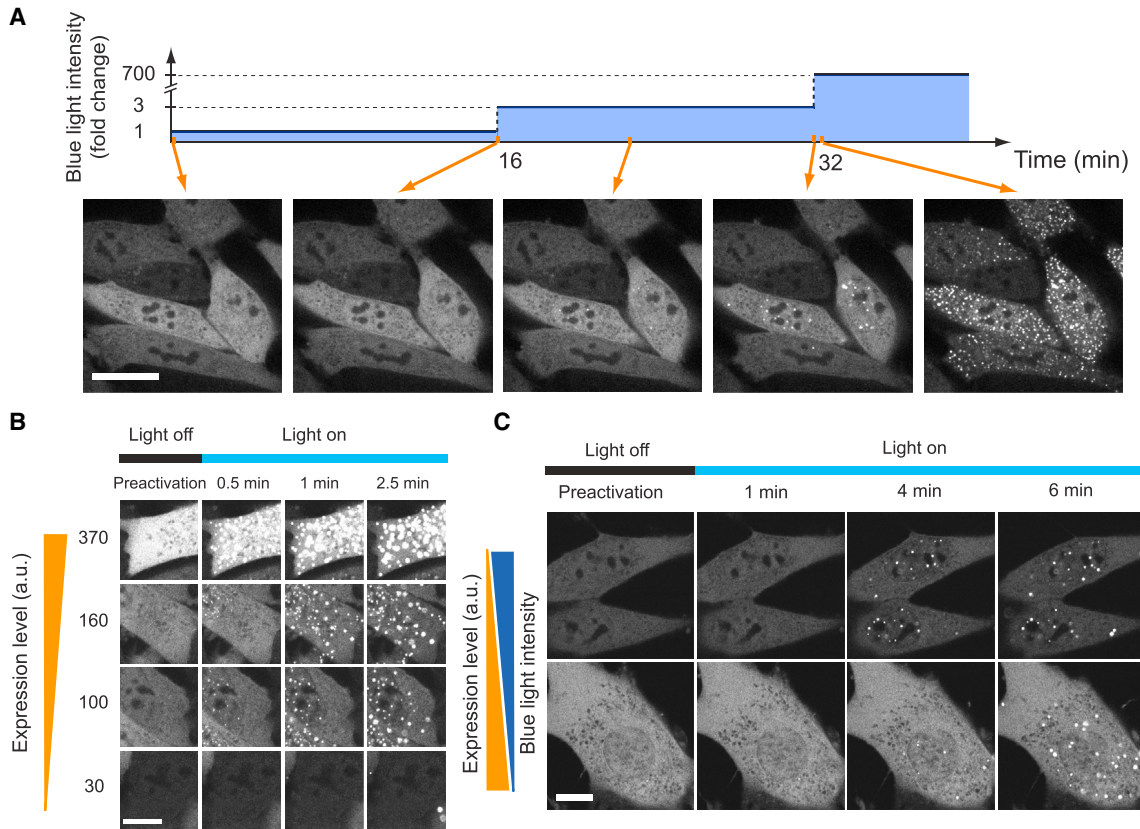


Figure 2. The Concentration of Activated Molecules Is a Key Determinant for Light-Activated Droplet Assembly

(A) Top: a sequence of increasing blue light intensity applied to optoFUS cells. Bottom: images of optoFUS cells taken during the activation sequence (time points indicated by arrows). Scale bar, 20 μ m. See also Movie S1.

(B) Images of optoFUS cells with varying expression levels (numeric values on the left, a.u.) exposed to identical blue light activation conditions. Scale bar, 10 μ m.

(C) Example images of optoFUS cells showing compensating effects of the expression level and blue light intensity. Cells with ~2-fold lower expression levels were activated with ~3.5-fold higher blue light intensity, yielding similar clustering kinetics. Scale bar, 10 μ m.

See also Figure S1.

fraction $F_{\text{inact,st}}$ of the total concentration: $C_{\text{inact,st}} = F_{\text{inact,st}}C_{\text{tot}}$, the steady-state background concentration is thus $C_{\text{bg,st}} = F_{\text{inact,st}}C_{\text{tot}} + C_{\text{sat}}$. Consistent with this model prediction, the steady-state background concentration of optoFUS cells increases linearly with total concentration (Figure 3C). Moreover, varying activation intervals yield different slopes ($F_{\text{inact,st}}$), but converge to a similar y-intercept (C_{sat}), corresponding to $\sim 1.4 \mu\text{M}$, consistent with the saturation concentration representing an intrinsic property of the optoFUS construct (Figure 3C). Indeed, the identical activation protocol, when applied to optoDDX4 cells, yields 2-fold lower C_{sat} (Figure S2D), implying stronger intermolecular interaction between DDX4 IDR.

We next sought to utilize this kinetic framework to quantify the rate constants for activation. We first computed the steady-state fraction of inactivated molecules for each cell using the relationship, $F_{\text{inact,st}} = (C_{\text{bg,st}} - C_{\text{sat}})/C_{\text{tot}}$, and the measured saturation concentration. In agreement with the model predictions, the fraction of inactivated molecules increases with either longer activation intervals or weaker blue light intensity (Figures 3D and S2A). This data can be well-fit to the functional dependence

predicted by the model, yielding values for the rate constants, $k_{\text{act}} = 7.4 \pm 4.7 \mu\text{W}^{-1}\text{s}^{-1}$ and $k_2 = 0.011 \pm 0.005 \text{ s}^{-1}$ (see the STAR Methods). Moreover, our data also agree with the model prediction that at high enough power, the inactivated fraction becomes independent of blue light intensity, because all molecules already populate the activated state (Figure 3D). Finally, phase separation should only occur if the total concentration of activated molecules exceeds the saturation concentration, C_{sat} . This prediction is in good agreement with our data, which show a sharp concentration threshold for the activated molecules, below which no cytoplasmic clusters are observed (Figure 3E).

Numerical Modeling of Light-Activated Liquid-Liquid Phase Separation

The above kinetic model provides a simple framework for quantifying the saturation concentration, which defines the phase boundary of the optoIDR system. To further understand the origin and dynamics of this light-activated phase separation process, we formulated a mesoscale continuum model. In this

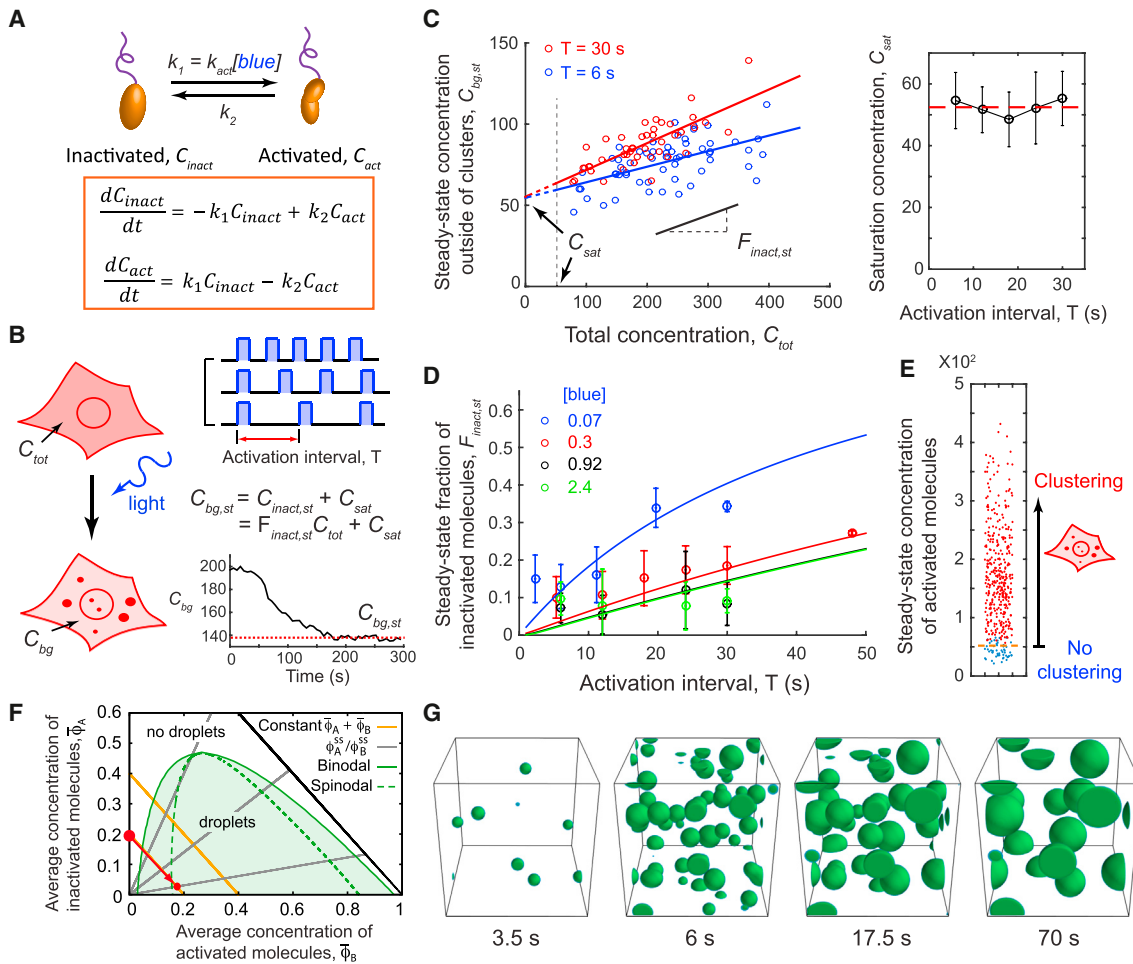


Figure 3. OptoFUS Clustering Is a Light-Activated Phase Transition

All experiments in this figure were performed with the optoFUS construct.

(A) Schematic diagram of light activation kinetics of Cry2. k_{act} and k_2 denote activation and inactivation rate constants, respectively. C_{act} and C_{inact} denote activated and inactivated molecule concentrations, respectively. Kinetic rate equations for light activation are given below the schematic.

(B) Light activation protocols with varying lengths of the activation interval, T , are employed to activate cells and temporal evolution of background fluorescence intensity outside of clusters, C_{bg} (black solid line in the example plot), is measured during clustering until it reaches steady state (red dotted line). $C_{inact,st}$ and $F_{inact,st}$ denote steady-state concentration and fraction of inactivated molecules, respectively. C_{tot} and C_{sat} represent total and saturation concentration, respectively.

(C) Left: steady-state background fluorescence intensities of individual cells (open circles) under the given activation interval increase linearly (solid lines) with total concentration of molecules. In our kinetic framework, the y intercept and the slope of the linear fit correspond to the saturation concentration, C_{sat} , and inactivated molecule fraction at steady state, $F_{inact,st}$, respectively. Right: the saturation concentration is independent of activation intervals used. A red dashed line represents average of saturation concentrations measured at five different activation intervals and error bars are 95% confidence intervals of linear fits.

(D) Steady-state fractions of inactivated molecules increase with either longer activation intervals or weaker blue light intensities. Blue light powers (488 nm, in μW) used in the measurements are specified. Solid lines denote a global fit to data using the kinetic model (see Equation 8 in the STAR Methods). Error bars, SDs.

(E) Steady-state concentrations of activated molecules for all cells examined were calculated using measured kinetic parameters, which show a clear concentration threshold for light-mediated clustering. A dotted horizontal line indicates the saturation concentration measured in (C).

(F) Phase diagram calculated using the mesoscale continuum model with $\chi_{AB} = -3$, $\chi_{AC} = -3$, $\chi_{BC} = 3.75$. The solid gold lines indicate two different expression levels of fixed $\bar{\phi}_A + \bar{\phi}_B$. The red circles and arrow highlight an example activation pathway through which phase separation is induced, and the solid gray lines are the line of steady-state concentration ratios preferred by the reaction terms for ($k_1 = 0.01$ and $T = 50$), ($k_1 = 0.01$ and $T = 17.5$) and ($k_1 = 0.2$ and $T = 75$) from top to bottom. The left-hand side of phase boundary represents the saturation concentration.

(G) Snapshots of droplet assembly from the simulation for the phase-transition pathway (red arrow) shown in (F).

See also Figures S2 and S3.

model, we describe the cytoplasm as a mixture of three chemical species; inactivated molecules of concentration $\phi_A(\vec{r})$, activated molecules of concentration $\phi_B(\vec{r})$, and all other cyto-

plasmic molecules at concentration $\phi_C(\vec{r})$; the fluid is incompressible such that $\phi_A + \phi_B + \phi_C = 1$. The free energy of the mixture is taken to be that of a ternary regular solution model,

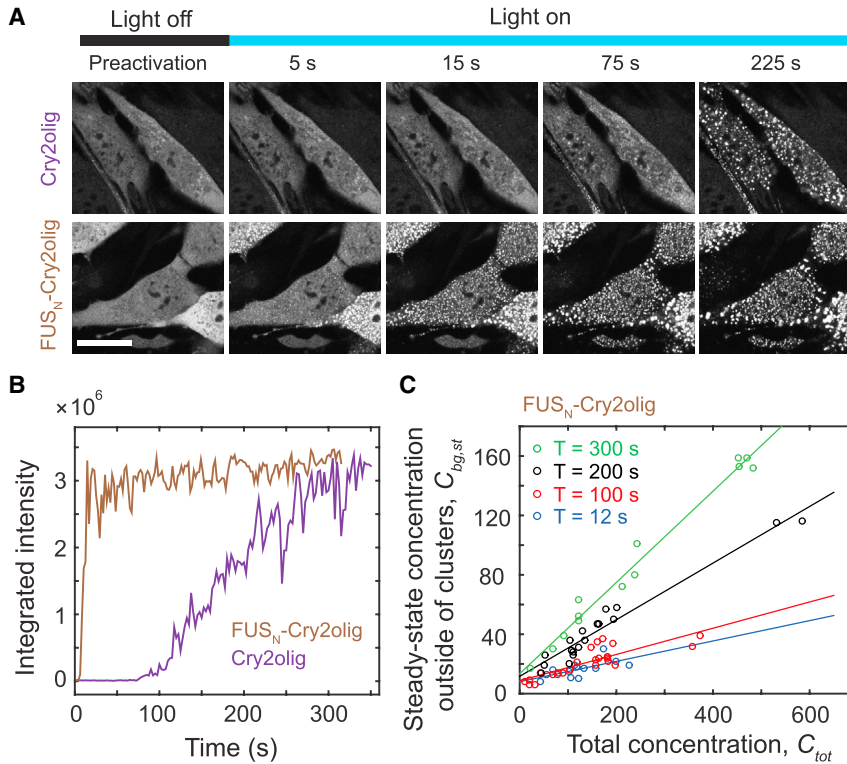


Figure 4. FUS_N-Cry2olig Shows Rapid Clustering with Lower Saturation Concentration Than optoFUS

(A) Time-lapse images of cells with Cry2olig and FUS_N-Cry2olig upon blue light activation. FUS_N fusion leads to rapid cluster assembly. Scale bar, 20 μ m.

(B) Temporal evolutions of integrated fluorescence intensity of cytoplasmic clusters for cells shown in (A).

(C) Steady-state background intensities of individual FUS_N-Cry2olig cells (open circles) under various activation intervals versus total concentration of molecules. The cyclic activation protocol identical to one used for optoFUS (Figures 3B and 3C) was applied for FUS_N-Cry2olig cells. Solid lines are linear fits to data, yielding 5-fold lower saturation concentration than optoFUS.

See also Figure S4.

background concentration are very similar to the experimental measurements (Figures S2C and S3A).

OptoDroplets Assembled with a Variant Light-Activation Domain

The preceding experiments and theoretical analysis show that fusing self-associating IDR's to the light activation domain

of Cry2WT enables light-activated phase separation. We wondered whether it is also possible to modulate the assembly dynamics by changing the light activation domain. Previously, a point mutant version of Cry2 (E490G), known as Cry2olig, was shown to exhibit significant clustering (Taslimi et al., 2014). We find that the assembly of Cry2olig is also dramatically enhanced when it is fused to FUS_N, exhibiting ~9-fold faster assembly under similar expression level and activation conditions (Figures 4A and 4B), which is comparable to the rapid assembly of our optoFUS construct (i.e., FUS_N-Cry2WT).

Applying the same method of cycled light activation described above (Figures 3B and 3C), we found that there is also a saturation concentration of FUS_N-Cry2olig (Figure 4C). However, the saturation concentration of FUS_N-Cry2olig is 5-fold lower than optoFUS, consistent with the point mutation (E490G) in Cry2olig increasing homo-interaction strength. Moreover, we found that the inactivation rate of FUS_N-Cry2olig is 5-fold slower than optoFUS (Figure S4A), consistent with the previous findings (Taslimi et al., 2014). These results suggest that utilizing IDR fusions with various other self-associating optogenetic proteins could be used to tune the dynamics of light-induced intracellular phase separation.

Rapid Growth and Fast Inactivation Lead to Localized Phase Separation

Local changes in molecular interaction strength can induce intracellular phase separation at specific subcellular locations, as in the case of P granule condensation during *C. elegans* embryo development (Brangwynne et al., 2009). We speculated that by

$$F[\phi_i(\vec{r})] = \int d\vec{r} \left[\phi_A \ln \phi_A + \phi_B \ln \phi_B + \phi_C \ln \phi_C + \chi_{AB} \phi_A \phi_B + \chi_{BC} \phi_B \phi_C + \chi_{AC} \phi_A \phi_C + \sum_i (\lambda_i \nabla \phi_i)^2 \right]$$

where $\chi_{ij}(\vec{r})$ define the strength of interaction between i and j molecules, and λ_i is the surface energy coefficient for population i; free energies of this type have been used in similar contexts (Lee et al., 2013; Berry et al., 2015). The first three terms represent the entropic contribution, which will tend to keep the system mixed. However, depending on the chosen interaction parameters χ_{ij} and average concentrations $\bar{\phi}_A$, $\bar{\phi}_B$, and $\bar{\phi}_C$, the equilibrium state may consist of a single uniformly mixed phase or the coexistence of two or three phases with differing average concentrations (see the STAR Methods).

The phase diagram for this ternary system highlights how intracellular phase space can be explored via modulation of blue light intensity, k_1 (Figure 3F). For a fixed expression level of optoFUS molecules ($\bar{\phi}_A + \bar{\phi}_B$), activation and inactivation reactions move the system through phase space along diagonals of constant $\bar{\phi}_A + \bar{\phi}_B$ (Figure 3F; gold lines). Phase separation is induced when an initially A-rich/B-poor system is activated with a sufficiently large light stimulus to cross the two-phase miscibility boundary (i.e., when the red arrow crosses the green phase boundary in Figure 3F), resulting in growing droplets as seen in Figure 3G. When the model is simulated with cyclic stimuli as in our experiments, the time evolution of the average species concentrations, oscillations and gradual decay in the

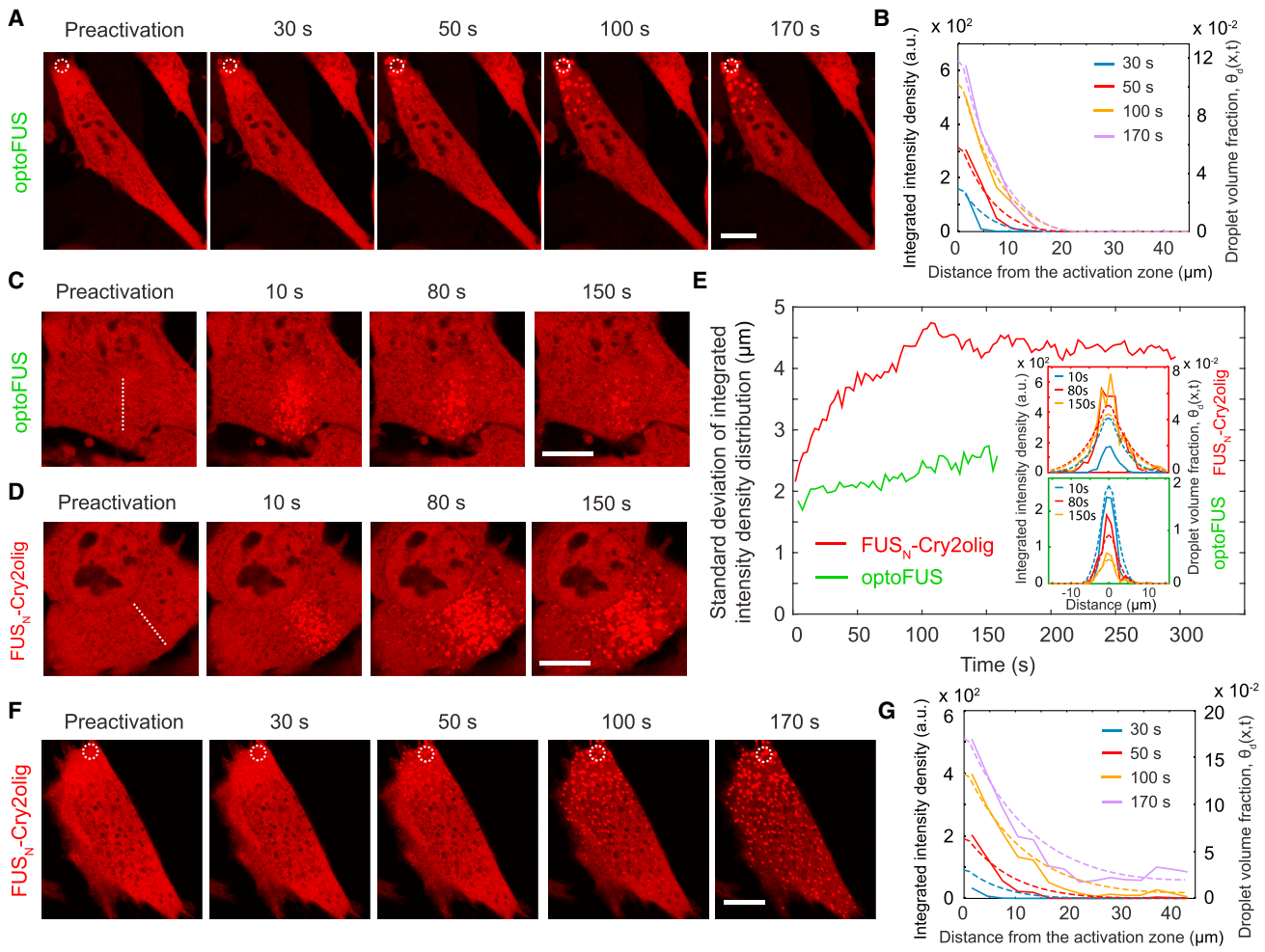


Figure 5. Localized Phase Transitions

(A) Time-lapse images of localized cluster formation for optoFUS. A circular area with a diameter of $1.9 \mu\text{m}$ (white dotted line) was periodically stimulated with blue light every 7.2 s. Scale bar, $10 \mu\text{m}$. See also [Movie S2](#).

(B) Temporal evolution of integrated intensity density of clusters versus distance away from the activation zone for clusters in (A). Solid lines are experimental data. Dashed lines are calculated droplet volume fraction profiles, $\theta_d(x,t)$, using coarse-grained phase-transition model (all parameters used in the calculation are listed in [Table S1](#)).

(C and D) Time-lapse images of optoFUS (C) and FUS_N-Cry2olig (D) showing clusters formed upon a single line activation (white dotted line). Scale bar, $10 \mu\text{m}$.

(E) Temporal evolution of standard deviations of integrated intensity density distributions for cells in (C) and (D). Insets: integrated intensity density distributions versus distance away from the activation zone for time points in (C) and (D). Solid lines are experimental data and dashed lines are droplet volume fraction profiles, $\theta_d(x,t)$, calculated using the coarse-grained phase-transition model (all parameters listed in [Table S1](#)).

(F) Time-lapse images of cluster wave formation upon localized activation of FUS_N-Cry2olig under the identical activation cycle used in (A). Scale bar, $10 \mu\text{m}$. See also [Movie S3](#).

(G) Temporal evolution of integrated intensity density of clusters versus distance away from the activation zone for clusters in (F). Solid lines are experimental data. Dashed lines are calculated droplet volume fraction profiles, $\theta_d(x,t)$, using coarse-grained phase-transition model (all parameters listed in [Table S1](#)). See also [Figures S5 and S6](#).

precisely controlling the spatial distribution of blue light, we may achieve analogous local phase separation. Consistent with this idea, when the corners of individual optoFUS cells were locally illuminated, droplets rapidly assembled near the activation zone, with a wave of droplet assembly propagating outward, but only over a short range near the activation zone ([Figures 5A and 5B; Movie S2](#)). We further verified this observation with single line activation, localized in time and space. When a line pulse was applied to optoFUS cells, droplets immediately form

along the activation line. The width of cluster distribution was maintained over a narrow band, before all droplets began disassembling within a few minutes ([Figures 5C and 5E](#)).

To quantitatively elucidate the dynamics of phase separation upon localized activation, we developed a simplified coarse-grained model that is consistent with the mesoscale model outlined above (see the [STAR Methods](#)). This model describes the concentration of activated molecules, $c(x)$, as well as the droplets they nucleate, which are characterized by the single

field variable $\theta_d(x,t)$ that represents the volume fraction of droplets within a given spatial volume. The model predicts that the steady-state droplet profile width for continuous localized activation is given by: $x_0^{ss} \sim \sqrt{D/k_2 \ln[k_1 E / (c_{sat} \sqrt{D(k_1 + k_2)})]}$, indicating that the primary factor is the reaction-diffusion length scale, $\sqrt{D/k_2}$, where D is the molecular diffusion coefficient in cytoplasm (see the [STAR Methods](#) for derivation and definition of E). Thus, diffusion of activated monomers will tend to oppose localized droplet formation, while rapid reversion to the dark state would sharpen droplet localization patterns. Numerical simulations of the model support this physical picture by reproducing the evolution time and extent of experimentally-observed droplet profiles, provided heterogeneous (seeded) nucleation kinetics are employed ([Figures 5B, 5E, and S5A](#)); interestingly, the observed behaviors are not consistent with homogeneous nucleation ([Figure S5A](#)).

Our coarse-grained model predicts that the 5-fold slower inactivation rate (k_2) and 5-fold lower C_{sat} exhibited by FUS_N -Cry2Olig relative to optoFUS would limit the ability to localize droplet assembly ([Figures S5B and S6](#)). Consistent with the model prediction, in FUS_N -Cry2Olig cells, clusters first rapidly appeared at the localized activation zone, but a wave of cluster formation then propagated slowly across the entire cell ([Figures 5F and 5G; Movie S3](#)); a single line pulse activation also displayed a broader cluster distribution than for optoFUS ([Figures 5D and 5E](#)). Moreover, cells expressing Cry2Olig alone exhibited a long lag time, followed by the concomitant appearance of clusters even far away from the activation zone ([Figures S5C–S5E](#)). These data demonstrate that localized phase separation depends critically on the rapid growth conferred by the IDR, combined with the relatively fast inactivation kinetics of Cry2WT.

Location in Phase Diagram Controls Material Properties and Aging Potential of Clusters

Our data show that optoIDR constructs are capable of undergoing light-activatable phase separation, but it is unclear whether the resulting clusters are liquid-like droplets, or more gel-like assemblies ([Kato et al., 2012; Patel et al., 2015; Murakami et al., 2015; Weber and Brangwynne, 2012; Zhang et al., 2015; Lin et al., 2015; Molliex et al., 2015](#)). Molecules within liquid phase droplets undergo dynamic exchange with the surrounding solution ([Brangwynne et al., 2009](#)). To probe the molecular dynamics of light-induced clusters, we performed fluorescence recovery after photobleaching (FRAP) experiments, by bleaching the mCherry signal ([Figure 6A](#)). For each of the cluster types assembled under weak light activation, we find a strong recovery of the fluorescence signal, with nearly complete recovery for optoFUS ($84\% \pm 16\%$ recovery) and optoHNRNPA1 ($84\% \pm 8\%$ recovery); optoDDX4 clusters exhibit slightly less recovery ($62\% \pm 9\%$ recovery). OptoFUS exhibits the fastest recovery timescale (137 ± 10 s), followed by optoHNRNPA1 (344 ± 40 s) and optoDDX4 (476 ± 50 s). Together, these data suggest that clusters formed upon blue light exposure are primarily liquid phase droplets, but can exhibit partially gel-like character. Interestingly, this behavior contrasts with the poor FRAP recovery of Cry2Olig and FUS_N -Cry2Olig clusters ([Figure 6A](#), purple, brown circles), which suggests that these are primarily gel-like structures. This is consistent with the very low saturation concentration of

FUS_N -Cry2Olig ([Figure S7A](#)) and the slow inactivation kinetics conferred by Cry2Olig.

Given these observations, we sought to determine if our optoDroplet system could be used to probe the emerging link between IDRs and liquid-to-solid transitions. In simple non-biological systems, moving deep into the two-phase region, corresponding to a high degree of supersaturation, can lead to condensation of assemblies with arrested dynamics, typically referred to as gels or glasses ([Lu et al., 2008; Zaccarelli, 2007](#)). We tested whether such arrested dynamics could be induced intracellularly, by exposing cells with similar optoFUS expression levels to varying intensities of blue light, thus moving to different depths beyond the phase boundary. For low light intensity such as that used in [Figure 6A](#) ($\sim 0.02 \mu\text{W}$, see the [STAR Methods](#)), which we refer to as “shallow” supersaturation, optoFUS cells typically show no clustering during a long lag period of ~ 100 s, followed by relatively slow phase separation ([Figure 6B](#)). As the light intensity increases, corresponding to increasing supersaturation, the lag period shortens; for sufficiently high blue light activation ($\sim 1.5 \mu\text{W}$, similar to laser powers typically used for low intensity GFP imaging), phase separation is initiated immediately after activation. Notably, shallow supersaturation conditions tend to give rise to relatively round droplet-like assemblies; in contrast, deep supersaturation leads over time to the formation of structures with more irregular shapes ([Figure 6C; Movie S4](#)). Small diffraction-limited puncta that appear immediately upon blue light exposure grow in size over time, in large part due to sticking to one another, forming highly branched, elongated structures ([Figure 6D](#)). FRAP measurements reveal that most molecules within these gel-like clusters do not exchange with the surrounding cytoplasm ([Figure 6E](#)). Indeed, as the supersaturation depth increases, the recovery fraction decreases, implying a larger immobile/solid fraction ([Figure 6F](#)).

To further probe the nature of the clusters formed at different locations within the phase diagram, we tested their disassembly dynamics upon turning off blue light. First, we note that without FUS_N , clusters of Cry2WT only form in a small subset of cells with high expression levels, but these disassemble relatively quickly ([Figures 6G and 6H, top row](#)). Upon turning off blue light, gel-like optoFUS clusters assembled from deep supersaturation also shrink in size, while maintaining their overall irregular morphology ([Movie S5](#)). However, they disassemble at a rate ~ 2.2 -fold slower than Cry2WT clusters, completely dissolving only after ~ 20 min ([Figure 6H](#)); this indicates that the self-associating FUS_N chains interact with sufficient strength to significantly delay dissolution. By contrast, under the shallow supersaturation condition, optoFUS droplets disassemble at a rate ~ 1.4 -fold faster than for deeply supersaturated optoFUS ([Figures 6G and 6H; middle row](#)). This suggests that the material state of clusters impacts the disassembly rate.

Several recent studies have shown that in vitro IDP liquid droplets undergo a transition into irreversible aggregates after multiple cycles of assembly and disassembly or prolonged incubation ([Murakami et al., 2015; Patel et al., 2015; Lin et al., 2015; Molliex et al., 2015; Zhang et al., 2015](#)). We find that when cells expressing optoFUS undergo a sequence of repeated cycles of shallow supersaturation, liquid-like optoFUS droplets fully dissolve each time blue light is turned off, even after three or

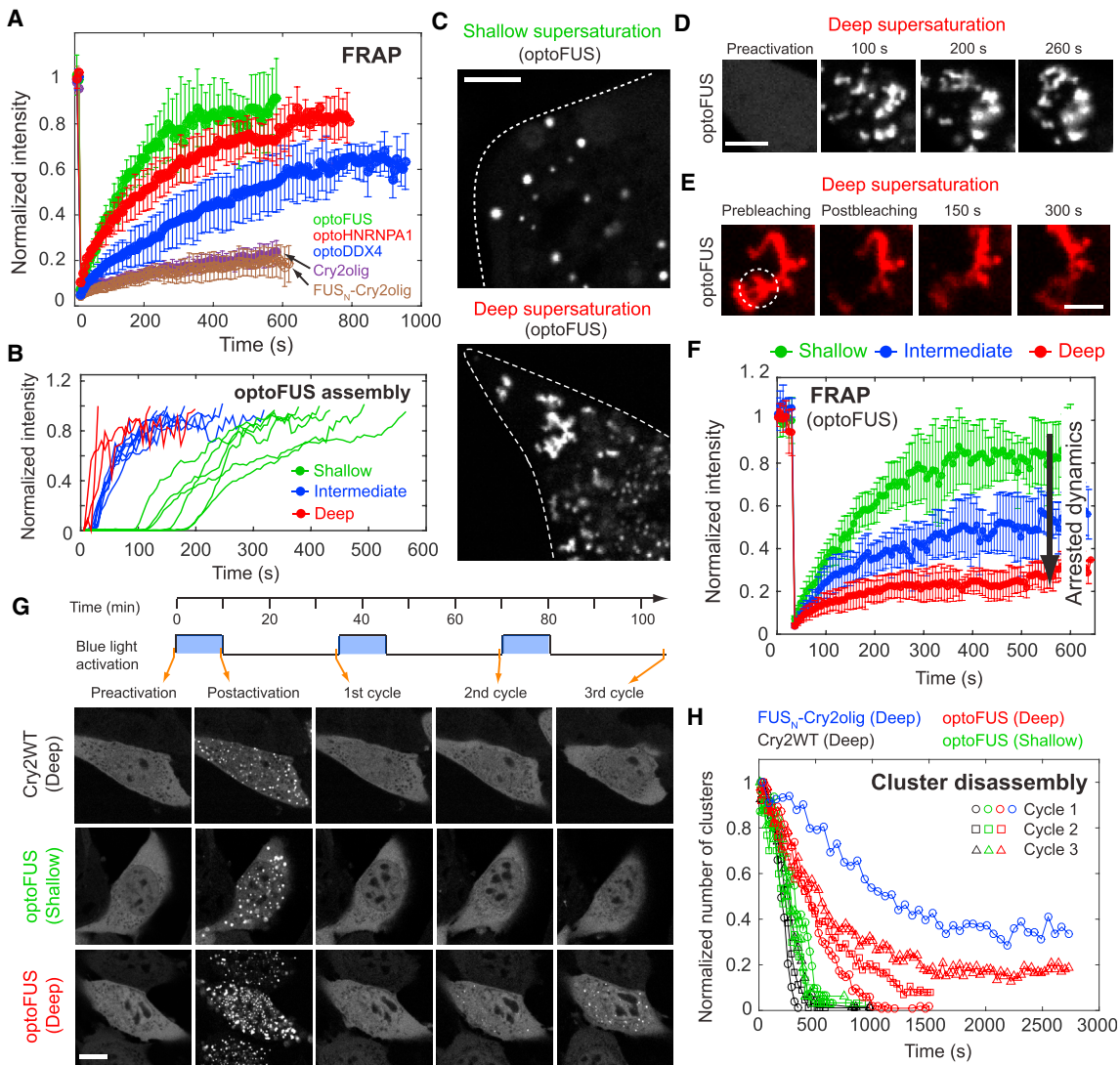


Figure 6. Material State and Reversibility of Light-Induced Clusters

- (A) FRAP recovery curves for optoIDRs and Cry2olig variants. Cells were activated every 6 s for 10 min with weak blue light ($\sim 0.02 \mu\text{W}$ except for optoDDX4 and FUS_N -Cry2olig where 20% and 70% further reduced powers are used to account for their lower C_{sat}) to induce phase separation. Error bars, SD ($n = 7-14$).
- (B) Normalized integrated intensities of light-induced optoFUS clusters for three different supersaturation depths (see the STAR Methods) after initiating blue light activation (time 0). Cells with similar expression levels are used. Integrated intensities were normalized with final values.
- (C) Distinct morphology of phase separated optoFUS clusters for shallow (top) and deep (bottom) supersaturation. Cell outlines are indicated with dashed lines. Scale bar, 5 μm . See also Movie S4.
- (D) Time-lapse images of optoFUS clusters forming upon deep supersaturation. Scale bar, 3 μm . See also Movie S4.
- (E) Example images of FRAP measurement for optoFUS gels. An optoFUS cell was activated every 6 s for 10 min with “deep” blue light condition. White dashed line indicates bleached area. Scale bar, 2 μm .
- (F) FRAP recovery curves of optoFUS clusters formed with varying supersaturation depths. The result for shallow activation is a replica of (A). Error bars, SD ($n = 8$ for both intermediate and deep).
- (G) Example images of Cry2WT and optoFUS cells under sequential cycles of assembly and disassembly. Cells are exposed to indicated blue light activation condition for 10 min to assemble clusters and then incubated in the absence of blue light for 25 min. Cell images before and after activation as well as at the end of each disassembly cycle are shown. Expression levels of these cells are similar. Scale bar, 10 μm .
- (H) Normalized number of clusters during disassembly cycles for cells in (G). The number of clusters for disassembly cycles was normalized with an initial cluster number for each cycle. FUS_N -Cry2olig data was added for comparison. Circles, squares, and triangles indicate the first, second, and third cycle, respectively. See also Figure S7.

more cycles (Figures 6G, 6H, and S7B). By contrast, when optoFUS cells are subjected to cycles of deep supersaturation, some clusters appear to remain as early as the end of the second cycle

(Figure 6G). By the third cycle, $\sim 20\%$ of clusters were not fully dissolved (Figures 6G, 6H, and S7B). Concomitantly, the disassembly rate of gel-like clusters gradually slows down over

subsequent cycles (Figure 6H). When tested up to five cycles, the number of remaining clusters increases progressively for each cycle (Movie S5). These aggregates are truly irreversible: after the cessation of light activation cycles, they remain assembled for at least 6 hr (Figure S7C).

One possible interpretation of these results is that irreversible cluster formation results from photophysical effects associated with light-sensitive Cry2WT. However, in control experiments under the same “deep” cyclic activation conditions, we do not observe any residual clusters for Cry2WT (no FUS fusion) constructs (Figure 6G). Nonetheless, we note that under longer activation conditions (after 3 hr of the high intensity illumination used for deep activation conditions), irreversible clusters can be induced in cells expressing Cry2WT alone (Figure S7D); when quantitatively compared, optoFUS forms irreversible aggregates at least 6-fold faster than Cry2WT (Figures S7F and S7G). Another possibility is that deep supersaturation conditions develop irreversible aggregates simply because more material has assembled into each cluster. However, we find that even when the total amount of phase-separated material is smaller than in cells with liquid droplets, cycles through the gel state robustly induce accumulation of irreversible aggregates (Figures S7E–S7G); this is consistent with the gel state providing a crucible for promoting irreversible aggregate formation. Interestingly, in cells expressing FUS_N-Cry2olig, irreversible clusters remain after just a single round of assembly (Figure 6H). Because FUS_N-Cry2olig clusters form gels even under shallow activation conditions (Figure 6A), prolonged incubation of molecules in the gel state due to the slow inactivation rate of Cry2olig may be enough to induce irreversible aggregate formation, even from a single activation cycle.

DISCUSSION

In this study, we have shown that phase transitions can be spatiotemporally controlled and probed within living cells using light. Our results show that the sticky IDRs of FUS, HNRNPA1, and DDX4 promote classical liquid-liquid phase separation within the cytoplasm of cultured cells, resulting in intracellular droplets that exhibit clear liquid signatures. Moreover, by precisely controlling the location within phase space, we identify and access additional material states of condensed intracellular phases, in particular more solid-like gels, which appear to age and nucleate irreversible aggregates. We also highlight physical parameters necessary for localized phase transitions, potentially used by cells to control the subcellular localization of membrane-less organelles.

The technique we have developed for controlling intracellular phase transitions is based on mimicking multivalent RNA binding proteins by fusing self-associating IDRs with a light-activatable Cry2(WT) motif. However, we note that other variants are likely possible (e.g., by fusing RNA binding domains to Cry2(WT) or fusing IDRs to other photoswitchable proteins) (Tischer and Weiner, 2014), which could be used to alter the assembly dynamics, wavelength-dependence, and material properties of these optoDroplets variants. Another potential strategy is to multimerize light-activatable motifs, which will have likely applications in controlling signaling clusters (Li et al., 2012). However,

it is likely that in order to recruit the full complement of proteins and RNA found within endogenous bodies, it may be necessary to fuse light-activatable domains to the full length protein.

Our approach is inspired by native mechanisms cells use to control phase transitions, which appear to be regulated in two distinct but complementary ways: (1) changing the concentration of molecules (e.g., by protein translation, altered degradation, or nucleocytoplasmic shuttling), and (2) changing their intermolecular interaction strengths (e.g., through PTMs, particularly phosphorylation that deposits a negative charge on the S, T, or Y residues that are common to IDRs driving phase separation). Indeed, FUS and HNRNPA1 are found in stress granules, one type of membrane-less body whose assembly depends on PTMs and protein concentration (Kedersha et al., 1999; Tourrière et al., 2003) and that have been suggested to assemble by regulated intracellular phase separation (Wippich et al., 2013; Mollieix et al., 2015; Patel et al., 2015). The assembly of other structures such as P granules, DDX4 puncta, and nucleoli also appear to be controlled through a combination of PTMs and protein concentration levels, which would similarly allow cells to move their cytoplasm into different regions of a high-dimensional phase diagram.

By dynamically tuning such protein interactions with light, we have achieved an unprecedented level of control over intracellular phase space, which we exploit to study the phase diagram within living cells. Focusing on assemblies driven by the N-terminal IDR of FUS, we find that varying the degree of supersaturation depth leads to clusters spanning different material states, ranging from liquid droplets to gels. Shallow supersaturation of optoFUS leads to liquid droplets, similar to those observed both *in vitro* and *in vivo* with FUS, HNRNPA1, DDX4, and other proteins. However, deep supersaturation results in the formation of gels, which exhibit minimal molecular dynamics and highly irregular aggregate-like morphologies.

These assemblies are reminiscent of gel-like structures previously observed *in vitro* for a variety of globular proteins (Dumetz et al., 2008; Muschol and Rosenberger, 1997). Notably, lysozyme, a well-folded protein whose phase behavior has been extensively studied *in vitro*, can undergo liquid-liquid phase separation, and deep within the two phase region can also exhibit arrested phase separation, with the condensed material forming a solid-like gel network (Cardinaux et al., 2007). The gel appears to represent a kinetically trapped state arising from the slow relaxation between strongly interacting molecules, rather than a thermodynamically favored state. Consistent with this, other reports have suggested that over time such gels can develop into crystals and fibers (Muschol and Rosenberger, 1997; Bucciantini et al., 2002).

Our data are thus in good agreement with a number of studies on the gelation of *in vitro* protein solutions. We have shown evidence that multiple cycles of intracellular optoFUS gel assembly lead to accumulation of irreversible aggregates. These findings echo a recent *in vitro* study, which showed that FUS hydrogels become irreversible after either long incubation or multiple temperature cycles (Murakami et al., 2015); similar cycle-dependent irreversibility was also seen with the ALS-related protein HNRNPA1 (Mollieix et al., 2015). The irreversible gel showed amyloid-like fiber morphologies, similar to inclusions

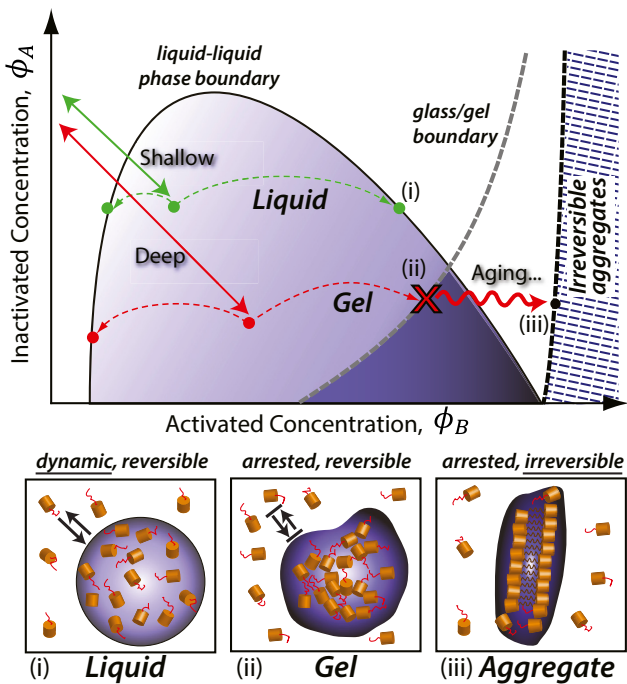


Figure 7. Model for Intracellular Phase Space

Conversion of molecular species from a weak self-association state to a high self-association state (e.g., through post-translational modification or exposure of RNA in RNP complexes) leads to liquid-liquid phase separation. When the depth is shallow, this process follows the green path to produce liquid droplets (i). Deep supersaturation along the red path results in the formation of solid-like gels with arrested molecular dynamics (ii). Gels are initially reversible, but slow dynamics within promote the formation of irreversible aggregates over time (iii).

found in patients with ALS and other neurodegenerative diseases. Although a detailed structural characterization of the nature of our intracellular optoFUS gels is beyond the scope of the present study, the irreversibility of aged aggregates may imply a molecular organization distinct from the initial gel state, and these structures could represent amyloid-rich assemblies.

Importantly, our data indicate that the gel state, but not the liquid state, promotes irreversible, and thus likely pathological, aggregates (Figure 7). This contrasts with several recent studies, highlighting liquid-to-solid transitions (Patel et al., 2015; Molliex et al., 2015; Lin et al., 2015; Zhang et al., 2015). In these primarily in vitro studies, the condensed liquid phase was believed to promote fibrous nuclei formation, often a rate-limiting step in amyloidogenesis. However, our data in living cells suggest that the severely slowed molecular dynamics inside the gel state may be important for promoting stable multi-protein contacts key for amyloid fiber assembly (Chiti and Dobson, 2009; Plakoutsi et al., 2005). Future studies will address these points by combining structural and cell biological characterization techniques with our versatile optoDroplet tool, utilizing a variety of IDRs in addition to those from FUS, HNRNPA1, and DDX4, which we have demonstrated here.

Taken together, our data suggests that increasing the strength or effective valency of molecular self-association (e.g., through light activation or endogenously through PTMs) can lead to

liquid-liquid phase separation, or for higher supersaturation can result in gelation. This is particularly interesting given many recent studies demonstrating membrane-less organelles with at least partially solid-like properties (i.e., viscoelasticity). For example, both nucleoli and stress granules have recently been reported to have a core-shell structure, where gel-like cores are engulfed by a dynamic liquid-like shell (Jain et al., 2016; Feric et al., 2016). Indeed, large variations in the immobile fraction of stress granule proteins are often measured in FRAP experiments (Guil et al., 2006; Mollet et al., 2008), and in some cases stress granules begin to resemble irregularly shaped gels (Kroschwald et al., 2015). We hypothesize that these apparent differences in the material state of native structures reflect different depths into the cytoplasmic phase diagram (Figure 7). This ability to tune material states by moving within the phase diagram is likely exploited by cells, because highly dynamic liquid-like states may be useful as microreactors, while gel-like structures would provide an ideal storage environment. However, our data suggest that assembling such arrested, gel-like structures deep within the phase diagram comes with the danger of producing potentially toxic species, due to irreversible aggregation and fibrillization. Exploring intracellular phase space with variants of our optoDroplet system will shed light on the strategies used by cells to organize the cytoplasm for proper function while also minimizing the associated danger of pathological aggregation.

STAR★METHODS

Detailed methods are provided in the online version of this paper and include the following:

- [KEY RESOURCES TABLE](#)
- [CONTACT FOR REAGENT AND RESOURCE SHARING](#)
- [EXPERIMENTAL MODEL AND SUBJECT DETAILS](#)
 - Cell culture
- [METHOD DETAILS](#)
 - Plasmid construction
 - Construction of stable cell lines
 - Live cell imaging
 - Estimation of absolute concentrations of mCh labeled constructs in cells
 - Control of supersaturation depth by modulating blue light intensity
 - Fluorescence recovery after photobleaching (FRAP)
- [QUANTIFICATION AND STATISTICAL ANALYSIS](#)
 - Image analysis
 - Kinetic modeling of light activation
 - Mesoscale model for light-induced liquid-liquid phase separation
 - Coarse-grained model for localized light-induced phase separation
 - Numerical methods

SUPPLEMENTAL INFORMATION

Supplemental Information includes seven figures, one table, and five movies and can be found with this article online at <http://dx.doi.org/10.1016/j.cell.2016.11.054>.

AUTHOR CONTRIBUTIONS

Y.S. generated constructs and cell lines, performed and analyzed data in all experiments, and developed the kinetic model. N.P. generated constructs and cell lines. J.B. and M.P.H. developed mesoscale and coarse-grained models and performed computational simulations and analysis. C.P.B., Y.S., and J.E.T. designed the study. C.P.B. and Y.S. wrote the paper with significant contributions from all authors.

ACKNOWLEDGMENTS

We thank members of the C.P.B. and J.E.T. laboratory for discussions. This work was supported by the NIH 4D Nucleome Program (U01 DA040601), as well as NIH Director's New Innovator Awards to C.P.B. (1DP2GM105437-01) and J.E.T. (1DP2EB024247-01). We also acknowledge funding from the Princeton Center for Complex Materials, an NSF-supported MRSEC (DMR 1420541), as well as an NSF CAREER award (1253035).

Received: May 31, 2016

Revised: September 20, 2016

Accepted: November 28, 2016

Published: December 29, 2016

REFERENCES

- Anderson, P., and Kedersha, N. (2009). RNA granules: post-transcriptional and epigenetic modulators of gene expression. *Nat. Rev. Mol. Cell Biol.* **10**, 430–436.
- Banerjee, R., Schleicher, E., Meier, S., Viana, R.M., Pokorny, R., Ahmad, M., Bittl, R., and Batschauer, A. (2007). The signaling state of *Arabidopsis* cryptochrome 2 contains flavin semiquinone. *J. Biol. Chem.* **282**, 14916–14922.
- Banjade, S., and Rosen, M.K. (2014). Phase transitions of multivalent proteins can promote clustering of membrane receptors. *eLife* **3**, e04123.
- Berry, J., Weber, S.C., Vaidya, N., Haataja, M., and Brangwynne, C.P. (2015). RNA transcription modulates phase transition-driven nuclear body assembly. *Proc. Natl. Acad. Sci. USA* **112**, E5237–E5245.
- Brangwynne, C.P., Eckmann, C.R., Courson, D.S., Rybarska, A., Hoege, C., Gharakhani, J., Jülicher, F., and Hyman, A. (2009). Germline P granules are liquid droplets that localize by controlled dissolution/condensation. *Science* **324**, 1729–1732.
- Brangwynne, C.P., Mitchison, T.J., and Hyman, A.A. (2011). Active liquid-like behavior of nucleoli determines their size and shape in *Xenopus laevis* oocytes. *Proc. Natl. Acad. Sci. USA* **108**, 4334–4339.
- Bucciantini, M., Giannoni, E., Chiti, F., Baroni, F., Formigli, L., Zurdo, J., Taddei, N., Ramponi, G., Dobson, C.M., and Stefani, M. (2002). Inherent toxicity of aggregates implies a common mechanism for protein misfolding diseases. *Nature* **416**, 507–511.
- Buchan, J.R., and Parker, R. (2009). Eukaryotic stress granules: the ins and outs of translation. *Mol. Cell* **36**, 932–941.
- Bugaj, L.J., Choksi, A.T., Mesuda, C.K., Kane, R.S., and Schaffer, D.V. (2013). Optogenetic protein clustering and signaling activation in mammalian cells. *Nat. Methods* **10**, 249–252.
- Burke, K.A., Janke, A.M., Rhine, C.L., and Fawzi, N.L. (2015). Residue-by-residue view of *in vitro* FUS granules that bind the C-terminal domain of RNA polymerase II. *Mol. Cell* **60**, 231–241.
- Cardinaux, F., Gibaud, T., Stradner, A., and Schurtenberger, P. (2007). Interplay between spinodal decomposition and glass formation in proteins exhibiting short-range attractions. *Phys. Rev. Lett.* **99**, 118301.
- Chiti, F., and Dobson, C.M. (2009). Amyloid formation by globular proteins under native conditions. *Nat. Chem. Biol.* **5**, 15–22.
- Dormann, D., and Haass, C. (2013). Fused in sarcoma (FUS): an oncogene goes awry in neurodegeneration. *Mol. Cell. Neurosci.* **56**, 475–486.
- Dumetz, A.C., Chockla, A.M., Kaler, E.W., and Lenhoff, A.M. (2008). Protein phase behavior in aqueous solutions: crystallization, liquid-liquid phase separation, gels, and aggregates. *Biophys. J.* **94**, 570–583.
- Elbaum-Garfinkle, S., Kim, Y., Szczepaniak, K., Chen, C.C.-H., Eckmann, C.R., Myong, S., and Brangwynne, C.P. (2015). The disordered P granule protein LAF-1 drives phase separation into droplets with tunable viscosity and dynamics. *Proc. Natl. Acad. Sci. USA* **112**, 7189–7194.
- Feric, M., and Brangwynne, C.P. (2013). A nuclear F-actin scaffold stabilizes ribonucleoprotein droplets against gravity in large cells. *Nat. Cell Biol.* **15**, 1253–1259.
- Feric, M., Vaidya, N., Harmon, T.S., Mitrea, D.M., Zhu, L., Richardson, T.M., Krivacki, R.W., Pappu, R.V., and Brangwynne, C.P. (2016). Coexisting liquid phases underlie nucleolar subcompartments. *Cell* **165**, 1686–1697.
- Guil, S., Long, J.C., and Cáceres, J.F. (2006). hnRNP A1 relocalization to the stress granules reflects a role in the stress response. *Mol. Cell. Biol.* **26**, 5744–5758.
- Handwerger, K.E., and Gall, J.G. (2006). Subnuclear organelles: new insights into form and function. *Trends Cell Biol.* **16**, 19–26.
- Ishimoto, C., and Tanaka, T. (1977). Critical behaviour of a binary mixture of protein and salt water. *Phys. Rev. Lett.* **39**, 8–11.
- Jain, S., Wheeler, J.R., Walters, R.W., Agrawal, A., Barsic, A., and Parker, R. (2016). ATPase-modulated stress granules contain a diverse proteome and substructure. *Cell* **164**, 487–498.
- Kato, M., Han, T.W., Xie, S., Shi, K., Du, X., Wu, L.C., Mirzaei, H., Goldsmith, E.J., Longgood, J., Pei, J., et al. (2012). Cell-free formation of RNA granules: low complexity sequence domains form dynamic fibers within hydrogels. *Cell* **149**, 753–767.
- Kedersha, N.L., Gupta, M., Li, W., Miller, I., and Anderson, P. (1999). RNA-binding proteins TIA-1 and TIAR link the phosphorylation of eIF-2 α to the assembly of mammalian stress granules. *J. Cell Biol.* **147**, 1431–1442.
- Kennedy, M.J., Hughes, R.M., Petreya, L.A., Schwartz, J.W., Ehlers, M.D., and Tucker, C.L. (2010). Rapid blue-light-mediated induction of protein interactions in living cells. *Nat. Methods* **7**, 973–975.
- Kroschwald, S., Maharana, S., Mateju, D., Malinovska, L., Nüske, E., Poser, I., Richter, D., and Alberti, S. (2015). Promiscuous interactions and protein disaggregases determine the material state of stress-inducible RNP granules. *eLife* **4**, e06807.
- Langer, J.S., and Schwartz, A.J. (1980). Kinetics of nucleation in near-critical fluids. *Phys. Rev. A* **21**, 948–958.
- Lee, C.F., Brangwynne, C.P., Gharakhani, J., Hyman, A.A., and Jülicher, F. (2013). Spatial organization of the cell cytoplasm by position-dependent phase separation. *Phys. Rev. Lett.* **111**, 088101.
- Lee, S., Park, H., Kyung, T., Kim, N.Y., Kim, S., Kim, J., and Heo, W.D. (2014). Reversible protein inactivation by optogenetic trapping in cells. *Nat. Methods* **11**, 633–636.
- Levskaya, A., Weiner, O.D., Lim, W.A., and Voigt, C.A. (2009). Spatiotemporal control of cell signalling using a light-switchable protein interaction. *Nature* **461**, 997–1001.
- Li, P., Banjade, S., Cheng, H.-C., Kim, S., Chen, B., Guo, L., Llaguno, M., Hollingsworth, J.V., King, D.S., Banani, S.F., et al. (2012). Phase transitions in the assembly of multivalent signalling proteins. *Nature* **483**, 336–340.
- Li, Y.R., King, O.D., Shorter, J., and Gitler, A.D. (2013). Stress granules as crucibles of ALS pathogenesis. *J. Cell Biol.* **201**, 361–372.
- Lin, Y., Protter, D.S.W., Rosen, M.K., and Parker, R. (2015). Formation and maturation of phase-separated liquid droplets by RNA-binding proteins. *Mol. Cell* **60**, 208–219.
- Lu, P.J., Zaccarelli, E., Ciulla, F., Schofield, A.B., Sciotino, F., and Weitz, D.A. (2008). Gelation of particles with short-range attraction. *Nature* **453**, 499–503.
- Mao, Y.S., Zhang, B., and Spector, D.L. (2011). Biogenesis and function of nuclear bodies. *Trends Genet.* **27**, 295–306.

- Mollet, S., Cougot, N., Wilczynska, A., Dautry, F., Kress, M., Bertrand, E., and Weil, D. (2008). Translationally repressed mRNA transiently cycles through stress granules during stress. *Mol. Biol. Cell* 19, 4469–4479.
- Mollieix, A., Temirov, J., Lee, J., Coughlin, M., Kanagaraj, A.P., Kim, H.J., Mittag, T., and Taylor, J.P. (2015). Phase separation by low complexity domains promotes stress granule assembly and drives pathological fibrillization. *Cell* 163, 123–133.
- Murakami, T., Qamar, S., Lin, J.Q., Schierle, G.S.K., Rees, E., Miyashita, A., Costa, A.R., Dodd, R.B., Chan, F.T.S., Michel, C.H., et al. (2015). ALS/FTD mutation-induced phase transition of FUS liquid droplets and reversible hydrogels into irreversible hydrogels impairs RNP granule function. *Neuron* 88, 678–690.
- Muschol, M., and Rosenberger, F. (1997). Liquid-liquid phase separation in supersaturated lysozyme solutions and associated precipitate formation/crystallization. *J. Chem. Phys.* 107, 1953–1962.
- Nott, T.J., Petsalaki, E., Farber, P., Jervis, D., Fussner, E., Plochowietz, A., Craggs, T.D., Bazett-Jones, D.P., Pawson, T., Forman-Kay, J.D., and Baldwin, A.J. (2015). Phase transition of a disordered nuage protein generates environmentally responsive membraneless organelles. *Mol. Cell* 57, 936–947.
- Patel, A., Lee, H.O., Jawerth, L., Maharana, S., Jahnel, M., Hein, M.Y., Stoynov, S., Mahamid, J., Saha, S., Franzmann, T.M., et al. (2015). A liquid-to-solid phase transition of the ALS protein FUS accelerated by disease mutation. *Cell* 162, 1066–1077.
- Phair, R.D., and Misteli, T. (2000). High mobility of proteins in the mammalian cell nucleus. *Nature* 404, 604–609.
- Plakoutsi, G., Bemporad, F., Calamai, M., Taddei, N., Dobson, C.M., and Chiti, F. (2005). Evidence for a mechanism of amyloid formation involving molecular reorganisation within native-like precursor aggregates. *J. Mol. Biol.* 351, 910–922.
- Ramaswami, M., Taylor, J.P., and Parker, R. (2013). Altered ribostasis: RNA-protein granules in degenerative disorders. *Cell* 154, 727–736.
- Sagui, C., and Grant, M. (1999). Theory of nucleation and growth during phase separation. *Phys. Rev. E* 59, 4175–4187.
- Schwartz, J.C., Cech, T.R., and Parker, R.R. (2015). Biochemical properties and biological functions of FET proteins. *Annu. Rev. Biochem.* 84, 355–379.
- Taslimi, A., Vrana, J.D., Chen, D., Borinskaya, S., Mayer, B.J., Kennedy, M.J., and Tucker, C.L. (2014). An optimized optogenetic clustering tool for probing protein interaction and function. *Nat. Commun.* 5, 4925.
- Tischer, D., and Weiner, O.D. (2014). Illuminating cell signalling with optogenetic tools. *Nat. Rev. Mol. Cell Biol.* 15, 551–558.
- Toettcher, J.E., Gong, D., Lim, W.A., and Weiner, O.D. (2011). Light-based feedback for controlling intracellular signaling dynamics. *Nat. Methods* 8, 837–839.
- Tourrière, H., Chebli, K., Zekri, L., Courselaud, B., Blanchard, J.M., Bertrand, E., and Tazi, J. (2003). The RasGAP-associated endoribonuclease G3BP assembles stress granules. *J. Cell Biol.* 160, 823–831.
- Van Genuchten, M.T., and Alves, W.J. (1982). Analytical Solutions of the One-Dimensional Convective-Dispersive Solute Transport Equation. Technical Bulletin 1661 (U.S. Department of Agriculture).
- Vekilov, P.G. (2010). Phase transitions of folded proteins. *Soft Matter* 6, 5254.
- Voorhees, P.W. (1992). Ostwald ripening of two-phase mixtures. *Annu. Rev. Mater. Sci.* 22, 197–215.
- Weber, S.C., and Brangwynne, C.P. (2012). Getting RNA and protein in phase. *Cell* 149, 1188–1191.
- Weber, S.C., and Brangwynne, C.P. (2015). Inverse size scaling of the nucleolus by a concentration-dependent phase transition. *Curr. Biol.* 25, 641–646.
- Wippich, F., Bodenmiller, B., Trajkovska, M.G., Wanka, S., Aebersold, R., and Peikmans, L. (2013). Dual specificity kinase DYRK3 couples stress granule condensation/dissolution to mTORC1 signaling. *Cell* 152, 791–805.
- Xiang, S., Kato, M., Wu, L.C., Lin, Y., Ding, M., Zhang, Y., Yu, Y., and McKnight, S.L. (2015). The LC domain of hnRNP A2 adopts similar conformations in hydrogel polymers, liquid-like droplets, and nuclei. *Cell* 163, 829–839.
- Zaccarelli, E. (2007). Colloidal gels: equilibrium and non-equilibrium routes. *J. Phys. Condens. Matter* 19, 323101.
- Zhang, H., Elbaum-Garfinkle, S., Langdon, E.M., Taylor, N., Occhipinti, P., Bridges, A.A., Brangwynne, C.P., and Gladfelter, A.S. (2015). RNA controls PolyQ protein phase transitions. *Mol. Cell* 60, 220–230.

STAR★METHODS

KEY RESOURCES TABLE

REAGENT or RESOURCE	SOURCE	IDENTIFIER
Chemicals, Peptides, and Recombinant Proteins		
FuGENE HD transfection reagent	Promega	Cat#E2311
GlutaMAX Supplement	ThermoFisher Scientific	Cat#35050061
In-Fusion HD Cloning Plus	Takara Bio USA	Cat#638909
Q5 Site-Directed Mutagenesis Kit	NEB	Cat#E0554S
Fibronectin Bovine Protein, Plasma	ThermoFisher Scientific	Cat#33010018
mCherry fluorescent protein	BioVision	Cat#4993-100
Experimental Models: Cell Lines		
NIH 3T3	ATCC	CRL-1658
293T Lenti-X	Takara Bio USA	Cat#632180
Recombinant DNA		
FUS ORF clone	GeneCopoeia	Cat# GC-F0952
pET9d-hnRNP-A1	Douglas Black	Addgene: 23026
Cry2olig-mCherry	Taslimi et al., 2014	Addgene: 60032
pHR-mCh-Cry2olig	This paper	N/A
pHR-mCh-Cry2WT	This paper	N/A
pHR-FUS _N -mCh-Cry2WT	This paper	N/A
pHR-DDX4 _N -mCh-Cry2WT	This paper	N/A
pHR-HNRNPA1 _C -mCh-Cry2WT	This paper	N/A
pHR-FUS _N -mCh-Cry2olig	This paper	N/A
Software and Algorithms		
ImageJ	NIH	https://imagej.nih.gov/ij/
MATLAB R2014b	Mathworks Inc., USA	http://www.mathworks.com

CONTACT FOR REAGENT AND RESOURCE SHARING

Further information and requests for reagents may be directed to, and will be fulfilled by the Lead Contact Clifford P. Brangwynne (cbrangwy@princeton.edu).

EXPERIMENTAL MODEL AND SUBJECT DETAILS

Cell culture

NIH 3T3 cells were cultured in 10% FBS (Atlanta Biological) in DMEM (GIBCO) supplemented with penicillin, streptomycin and GlutaMAX (Thermo) at 37°C with 5% CO₂ in a humidified incubator.

METHOD DETAILS

Plasmid construction

DNA fragments encoding IDRs of human FUS (residues 1-214) and human HNRNPA1 (residues 186-320) were amplified by PCR using FUS cDNA (GeneCopoeia) and pET9d-hnRNP-A1 (Addgene), respectively. A gene for the IDR of human DDX4 (residues 1-236) was synthesized (Integrated DNA Technologies). Sequences for mCherry and Cry2olig (Addgene) were cloned into the pHRS lentiviral backbone to generate the pHRS-mCh-Cry2olig plasmid. A site-directed mutagenesis (NEB) was then performed to produce the Cry2WT version. For IDR-fusion Cry2 plasmids, DNA fragments encoding the IDRs were inserted into the linearized pHRS-mCh-Cry2WT (or Cry2olig) backbone using In-Fusion Cloning Kit (Takara). The resulting constructs were fully sequenced to confirm the absence of unwanted substitutions.

Construction of stable cell lines

To produce stable cell lines expressing Cry2 fusion constructs, lentiviral constructs were transfected with FuGENE (Promega), following the manufacturer's recommended protocol, into 293T cells that had been plated in the 6-well dishes 1 day prior to the transfection. Viral supernatants were collected 2 d after transfection and passed through a 0.45- μm filter to remove cell debris. NIH 3T3 cells plated at ~70% confluence in the 6-well dishes were infected by adding 0.4–1 mL of filtered viral supernatant directly to the cell medium. Viral medium was replaced with normal growth medium 24 hr after infection.

Live cell imaging

35-mm glass-bottom dishes (MatTek) were coated for 20 min with 0.25 mg/ml fibronectin (Thermo) and then washed twice with PBS (pH 7.4, Thermo). Cells were plated on the fibronectin coated dish and grown typically overnight in normal growth medium to reach ~50% confluence. Just prior to imaging, the medium was replaced with imaging medium consisting of 2% FBS in HBSS (Corning cellgro). All live cell imaging was performed using 60X oil immersion objective (NA 1.4) on a Nikon A1 laser scanning confocal microscope equipped with a temperature stage at 37°C. For global activation, cells were imaged typically by use of two laser wavelengths (488 nm for Cry2 activation /560 nm for mCherry imaging). To execute activation protocols with varying activation intervals, the repetitive ON/OFF cycle was applied by varying the length of OFF time (the activation duration, t_a , was fixed to 1 s in all measurements). Localized activation experiments were performed using the stimulation setting where the blue laser scans only a designated region of interest.

Estimation of absolute concentrations of mCh labeled constructs in cells

Recombinant mCherry (Biovision) was reconstituted to 1 mg/ml ($= 34.7 \mu\text{M}$) and a series of dilutions were imaged with identical imaging conditions used for 3T3 cells with mCh labeled constructs. A standard curve relating pixel intensity, I, to concentration, [mCh], was obtained, yielding $I = a[mCh]$ with $a = 36 / \text{pixel} \cdot \mu\text{M}$. With this conversion factor, we estimated the intracellular concentration of mCh labeled constructs used in our study ranging from 0.2 - 13 μM and the saturation concentration of optoFUS (FUS_N-Cry2WT) and FUS_N-Cry2olig to be 1.4 μM and 0.3 μM , respectively.

Control of supersaturation depth by modulating blue light intensity

We found that blue light mediated activation of Cry2 is highly sensitive and even the lowest 440 or 488 nm laser setting in our confocal microscope, corresponding to ~0.1 μW (measured with optical power meter PM100D, Thorlabs), is sufficient to drive rapid phase separation of optoIDR constructs. To further decrease blue light intensity, 440 nm activation is used in conjunction with the dichroic mirror for 488 nm, leading to ~50-fold attenuation in blue light intensity at the specimen plane. With this method, a broad range of the 440 nm laser power was delivered on the sample, covering three distinct activation conditions used in our study to control supersaturation depths. The blue light power of ~0.02 μW , ~0.06 μW and ~1.5 μW were used for shallow, intermediate and deep activation condition, respectively (Figures 6 and S7). We note that the reported blue light absorption of Cry2 at 488 nm is ~70% of that at 440 nm (Banerjee et al., 2007) and the light dose curve (Figure 3D) corresponds to intermediate to deep supersaturation conditions.

Fluorescence recovery after photobleaching (FRAP)

Cells were first globally activated by dual color imaging every 6 s for 10 min with an appropriate blue light intensity to reach a desirable supersaturation depth. Immediately after termination of the activation phase, light-induced clusters were bleached with a spot of ~1.5 μm in diameter and their fluorescence recovery was monitored while maintaining identical activation conditions used to induce clustering. Intensity traces were collected using ImageJ, corrected for photobleaching and normalized with pre-bleaching intensity.

QUANTIFICATION AND STATISTICAL ANALYSIS

Statistical parameters are indicated in the legends of each figure, including the definitions of error bars (e.g., standard deviation (SD), 95% confidence intervals, etc) and the number experimental replication, denoted by "n."

Image analysis

Total concentrations of molecules as well as steady-state background concentrations outside clusters were measured from fluorescence images of cells using ImageJ (NIH), and corrected by subtracting background noises measured with areas absent from any cells. Custom written MATLAB (Mathworks Inc) scripts were used for all other image analysis including detection of clusters and quantification of assembly/disassembly dynamics. Briefly, raw images were Gaussian filtered to reduce high frequency noise and then clusters were detected based on their peak intensity. Detected clusters in each movie were examined manually to confirm their validity. Cell and nucleus peripheries were manually identified and only cytoplasmic clusters were analyzed subsequently. To quantify the total amount of phase separated materials for each frame, all cytoplasmic pixel intensities three standard deviations above the average background intensity outside clusters were integrated.

Kinetic modeling of light activation

The analytic expression for steady-state average fractions of activated molecules under a given cyclic activation protocol (Figure 3B) was solved to fit experimental data. First, the first-order light activation model (shown in Figure 3A, rewritten here in a matrix form) was solved for a single round of blue light ON/OFF.

$$\frac{d}{dt} \begin{pmatrix} F_{inact} \\ F_{act} \end{pmatrix} = \begin{pmatrix} -k_1 & k_2 \\ k_1 & -k_2 \end{pmatrix} \begin{pmatrix} F_{inact} \\ F_{act} \end{pmatrix} \quad (1)$$

where F_{inact} and F_{act} denote fractions of inactivated and activated molecules, respectively. In addition, k_2 denotes an inactivation rate constant and we refer to k_1 as a forward reaction constant in order to distinguish it from an activation rate constant, k_{act} , ($k_1 = k_{act}/[blue]$, where $[blue]$ is a blue light intensity). For the ON time, both activation and inactivation reactions occur but, during the OFF time, only activated molecules convert to the inactivated state. For the activation protocol with the activation interval, T , and the ON time, t_a , the fractions of molecules in each state after the first round of ON/OFF cycle is given by,

$$\begin{pmatrix} F_{inact} \\ F_{act} \end{pmatrix}_{t=t_a} = \frac{1}{k_1 + k_2} \begin{pmatrix} k_2 + k_1 e^{-(k_1 + k_2)t_a} & k_2 - k_1 e^{-(k_1 + k_2)t_a} \\ k_1 - k_1 e^{-(k_1 + k_2)t_a} & k_1 + k_2 e^{-(k_1 + k_2)t_a} \end{pmatrix} \begin{pmatrix} F_{inact} \\ F_{act} \end{pmatrix}_{t=0} \quad (2)$$

$$\begin{pmatrix} F_{inact} \\ F_{act} \end{pmatrix}_{t=T} = \begin{pmatrix} 1 & 1 - e^{-k_2(T-t_a)} \\ 0 & e^{-k_2(T-t_a)} \end{pmatrix} \begin{pmatrix} F_{inact} \\ F_{act} \end{pmatrix}_{t=t_a} = P \begin{pmatrix} F_{inact} \\ F_{act} \end{pmatrix}_{t=0} \quad (3)$$

where P is a 2×2 matrix whose elements are functions of k_1 , k_2 , T , t_a . After the n -th activation cycle, the fractions of molecules are then simply given by the n -th power of P ,

$$\begin{pmatrix} F_{inact} \\ F_{act} \end{pmatrix}_{t=nT} = P^n \begin{pmatrix} F_{inact} \\ F_{act} \end{pmatrix}_{t=0}. \quad (4)$$

Using matrix diagonalization,

$$\begin{pmatrix} F_{inact} \\ F_{act} \end{pmatrix}_{t=nT} = Q \Lambda^n Q^{-1} \begin{pmatrix} F_{inact} \\ F_{act} \end{pmatrix}_{t=0} \quad (5)$$

where Q is a 2×2 matrix whose columns are eigenvectors of P and Λ is a 2×2 diagonal matrix with eigenvalues of P . Solving Equation 5 leads to the fraction of activated molecules after the n -th cycle,

$$(F_{act})_{t=nT} = \frac{k_1}{k_1 + k_2} \frac{e^{(k_1 + k_2)t_a} - 1}{e^{k_2 T + k_1 t_a} - 1} (1 - e^{-n(k_2 T + k_1 t_a)}). \quad (6)$$

At steady state, the fraction of activated molecules after the disassembly (OFF) phase is thus given as

$$(F_{act,st})_{OFF} = \frac{k_1}{k_1 + k_2} \frac{e^{(k_1 + k_2)t_a} - 1}{e^{k_2 T + k_1 t_a} - 1}. \quad (7)$$

Since there are still oscillations in the fractions of molecules even at steady state due to repeated cycles of ON and OFF phases (Figures S2A–S2C), we computed average fractions of molecules, time averaging over single ON/OFF cycle at steady state, to fit the steady-state fraction of inactivated molecules, $(F_{inact,st})_{av} = 1 - (F_{act,st})_{av}$, (Figure 3D),

$$(F_{act,st})_{av} = \frac{k_1}{k_1 + k_2} \frac{e^{(k_1 + k_2)t_a} - 1}{e^{k_2 T + k_1 t_a} - 1} \left\{ \frac{t_a}{T} - (e^{k_2(T-t_a)} - 1) \left[\frac{1}{(k_1 + k_2)T} + \frac{t_a}{T(e^{-(k_1 + k_2)t_a} - 1)} - \frac{1}{k_2 T} \right] \right\}. \quad (8)$$

For continuous activation ($T = t_a$), this expression reduces to a simple form,

$$(F_{act,st})_{av} = \frac{k_1}{k_1 + k_2}. \quad (9)$$

Thus, steady-state fractions of Cry2 states are solely dependent on kinetic rates and activation protocols. Together with the simple relation ($C_{bg,st} = F_{inact,st} C_{tot} + C_{sat}$) described in the main text, the model predicts that the steady-state background concentration will exhibit, under a fixed activation protocol, a linear dependence on the total concentration in the cell, with a y intercept equal to the saturation concentration (Figure 3C). Direct measurement of $C_{bg,st}$ and C_{tot} from fluorescence images of individual cells allows quantification of kinetic rates as well as saturation concentration.

Mesoscale model for light-induced liquid-liquid phase separation

The interaction parameters χ_{ij} in the ternary regular solution free energy equation, shown in the main text, are chosen such that for sufficient concentration of activated B molecules, the system undergoes a phase transition from a uniformly mixed fluid to a mixture

of B-rich (droplet) and B-poor (background) phases (Figure 3F). Dynamics of the dimensionless molecular concentration fields ϕ_i are assumed to be diffusive, while laser-induced activation and spontaneous inactivation processes are treated as first-order chemical reactions, consistent with the kinetic framework described in the main text and in the kinetic modeling section above;

$$\begin{aligned}\partial_t \phi_A(\vec{r}) &= M_A \nabla^2 \frac{\delta F}{\delta \phi_A} - k_1(\vec{r}, t) \phi_A + k_2 \phi_B + \eta_A \\ \partial_t \phi_B(\vec{r}) &= M_B \nabla^2 \frac{\delta F}{\delta \phi_B} + k_1(\vec{r}, t) \phi_A - k_2 \phi_B + \eta_B.\end{aligned}\quad (10)$$

Here M_i is the mobility of species i , t is dimensionless time, and $k_1(\vec{r}, t)$, k_2 are the rate parameters in the first order chemical reaction $A \xrightleftharpoons[k_2]{k_1} B$. The last term in Equation 10 accounts for molecular-scale processes in a stochastic way, by averaging them into uncorrelated Gaussian fluctuations specified by mean $\langle \eta_i \rangle = 0$ and correlation $\langle \eta_i(\vec{r}_1, t_1) \eta_j(\vec{r}_2, t_2) \rangle = -2k_B T M_i \nabla \cdot \nabla \delta(\vec{r}_1 - \vec{r}_2) \delta(t_1 - t_2)$.

Interestingly, the phase diagram for the ternary regular solution system suggests that the saturation concentration may actually vary with the total concentration, depending on the shape of the phase boundary (the left-hand side of green phase boundary in Figure 3F). Nonetheless, an analysis of this effect shows good agreement with our observations of a clear concentration threshold for phase separation (Figures S3B and S3C).

Coarse-grained model for localized light-induced phase separation

Our coarse-grained model for droplet kinetics under localized activation describes how the local volume fraction of droplet phase, $\theta_d(x, t)$, evolves in concert with the concentration of activated molecules in the background phase, $C_{act,bg}(x, t)$. Averaging over y and z directions for a simplified 1D description, the model reads

$$\begin{aligned}\frac{dc}{dt} &= D \frac{d^2 c}{dx^2} + k_1(x, t)[1 - c_{tot}(x, t)] - k_2 c(x, t)(1 - \theta_d) - (c_d - c) \frac{d\theta_d}{dt} \\ \frac{d\theta_d}{dt} &= \frac{d\theta_d^0}{dt} - k_2 \theta_d \\ \frac{d\theta_d^0}{dt} &= \frac{d}{dt} \left[\int_0^t dt' J(t') \frac{4\pi}{3} R^3(t-t') \right]\end{aligned}\quad (11)$$

where D is the diffusion coefficient of activated molecules in the background phase, and the concentrations of activated molecules are all scaled by the initial uniform concentration of inactivated molecules, C_0 (expression level). These are $c = C_{act,bg}(x, t)/C_0$ in the background phase, $c_d = C_{act,d}/C_0$ in the droplet phase in equilibrium, and $c_{tot}(x, t) = c(1 - \theta_d) + c_d \theta_d$ in total. The first equation quantifies how, upon localized activation (2nd term R.H.S.), the accumulation of activated molecules is opposed by three factors: i) diffusive spreading (1st term R.H.S.), ii) by inactivation (3rd term R.H.S) and iii) the nucleating and growing droplet phase acting as a sink (4th term R.H.S.).

The second equation describes how the droplet phase changes over time; it can grow and shrink. The rate of shrinkage is assumed to be equal to the inactivation rate. The third equation represents the growth of the droplet phase; the growing droplet phase, θ_d^0 , is given by the integral of the droplet nucleation rate $J(t)$ multiplied by the volume of droplet phase $V = 4\pi R^3(t)/3$, where R is droplet radius. $J(t)$ is determined from classical nucleation theory for both heterogeneous $J_{het}(t)$ and homogeneous $J_{hom}(t)$ nucleation mechanisms. $R(t)$ is assumed to follow diffusion-limited growth kinetics, where $dR/dt = DS(t)/R$ and $S(t) = S_0(c - c_{sat})$ is the supersaturation with prefactor S_0 . Parameters used in the simulation are listed in Tables S1 and S2.

Heterogeneous nucleation was treated in Equation 11 by assigning $J_{het}(t) = n\delta(t)$, where n is the density of nucleation sites and $\delta(t)$ is the Dirac delta function. A fixed number of droplets, set by n , thus instantaneously nucleate at the time at which $c(x)$ first reaches c_{sat} . For homogeneous nucleation, we employed the 3D field-theoretic steady-state nucleation rate (Langer and Schwartz, 1980; Sagu and Grant, 1999), which in dimensionless form is $J_{hom}(t) = \frac{3}{4\pi} \chi_0^6 S^{2/3}(t) [1 + S(t)]^{3.55} e^{-1/S^2(t)}$ where $\chi_0 = (4\pi\gamma_c^2/3k_B T)^{1/2}$ and γ is the surface tension. The characteristic length in this representation is the capillary length $l_c = 2\gamma V_m/k_B T$, where V_m is the molecular volume, and the characteristic time is $t_c = l_c^2/D c_{eq}(\infty) V_m$, where $c_{eq}(\infty)$ is the solute concentration infinitely far away from a planar interface in equilibrium. Homogeneous nucleation rates decrease dramatically with local supersaturation ($J_{hom} \sim e^{-1/S^2}$), which leads to greatly

enhanced nucleation and growth within and near the activation zone (Figure S5A). For the physical conditions relevant to this study, the droplet profile width during homogeneous nucleation was found to remain on the order of the width of the activation zone itself (Figure S5A).

Analytical solution procedures

When condensation of activated molecules into droplets is not too strong and/or rapid relative to diffusive spreading ($d\theta_d/dt \rightarrow 0$ and/or $c_d\theta_d \ll 1$), Equation 11 reduces to the evolution equation for a diffusing concentration field $c(x,t)$ with first-order decay and a saturating zeroth-order source,

$$\frac{dc}{dt} = D \frac{d^2c}{dx^2} + k_1(x)(1 - c) - k_2c. \quad (12)$$

For $k_1(x) = k_1$ over $-L < x < L$ and $k_1(x) = 0$ otherwise, with boundary conditions $dc(\infty, t)/dx = 0$ (no walls), the steady-state solution obtained by separation of variables is

$$c_{ss}(x) = \begin{cases} \bar{k}\lambda_1 e^{\lambda_0(L+x)} \frac{\lambda_- e^{-\lambda_1 L} + \lambda_+ e^{3\lambda_1 L} - 2\lambda_0 e^{\lambda_1 L}}{\lambda_+^2 e^{3\lambda_1 L} - \lambda_-^2 e^{-\lambda_1 L}} & x \leq -L \\ \bar{k} \frac{2\lambda_0 \cosh(\lambda_1 x) (\lambda_+ e^{2\lambda_1 L} - \lambda_-) - \lambda_+^2 e^{3\lambda_1 L} + \lambda_-^2 e^{-\lambda_1 L}}{\lambda_+^2 e^{3\lambda_1 L} - \lambda_-^2 e^{-\lambda_1 L}} & -L < x < L \\ \bar{k}\lambda_1 e^{\lambda_0(L-x)} \frac{\lambda_- e^{-\lambda_1 L} + \lambda_+ e^{3\lambda_1 L} - 2\lambda_0 e^{\lambda_1 L}}{\lambda_+^2 e^{3\lambda_1 L} - \lambda_-^2 e^{-\lambda_1 L}} & x \geq L \end{cases} \quad (13)$$

where $\bar{k} = k_1/(k_1 + k_2)$, $\lambda_0 = l_0^{-1}$, $\lambda_1 = l_1^{-1}$, $\lambda_+ = \lambda_0 + \lambda_1$, $\lambda_- = \lambda_0 - \lambda_1$, $l_0 = \sqrt{D/k_2}$, and $l_1 = \sqrt{D/(k_1 + k_2)}$.

The time for $c(x,t) \rightarrow c_{ss}(x)$ is on the order of $1/k_2$. If significant droplet growth has not occurred by this time, we may approximate the maximum width x_0^{ss} of the droplet forming zone as that corresponding to the extent over which $c_{ss}(x)$ exceeds c_{sat} . Applying this reasoning and solving $c_{ss}(x \geq L) = c_{sat}$ for x gives

$$x_0^{ss} = l_0 \ln \left[\frac{\bar{k}E}{c_{sat}l_1} \right] + L \quad (14)$$

where $E = (2\lambda_0 e^{\lambda_1 L} - \lambda_- e^{-\lambda_1 L} - \lambda_+ e^{3\lambda_1 L}) / (\lambda_-^2 e^{-\lambda_1 L} - \lambda_+^2 e^{3\lambda_1 L})$, and $2L$ is the width of the activation zone.

Numerically simulated steady-state θ_d profiles are well-described by this expression when the $c \rightarrow c_{ss}$ limit is sufficiently realized (generally, large k_2 , c_{sat} / small D , k_1 ; see below). Results indicate that this limit is not fully realized in optoFUS and FUS_N-Cry2olig systems, as diffusive spreading and droplet growth are found to occur on comparable timescales, but Equation 14 nonetheless provides physical insight and fair quantitative guidance. For example, it indicates that the width of the droplet-forming zone is primarily controlled by the length scale $l_0 = \sqrt{D/k_2}$, with somewhat weaker dependences on k_1 and c_{sat} which enter only within the logarithm. It also reasonably predicts a ratio of olig to WT profile widths of $\sim 3.5:1$. The 5-fold difference in k_2 accounts for a factor of ~ 2 ($l_0 \sim 25 \mu\text{m}$ versus $\sim 60 \mu\text{m}$), and the 4-to-5-fold difference in c_{sat} contributes another factor of ~ 1.5 .

A fully time-dependent solution for $c(x, t)$ can be obtained for the case in which the effect of k_1 is replaced with the time-dependent boundary condition $c(0, t) = c_0(1 - e^{-\lambda t})$. This is approximately the behavior expected within the activation zone, where c saturates to some maximum value c_0 over a timescale $1/\lambda \approx 1/k_1$. The solution for $c(x, t)$ obtained by Laplace transforms (Van Genuchten and Alves, 1982) is

$$c(x, t) = \frac{c_0}{2} \left[e^{-Ux/2D} \operatorname{erfc} \left(\frac{x - Ut}{2\sqrt{Dt}} \right) + e^{Ux/2D} \operatorname{erfc} \left(\frac{x + Ut}{2\sqrt{Dt}} \right) \right] - \frac{c_0 e^{-\lambda t}}{2} \left[e^{-Wx/2D} \operatorname{erfc} \left(\frac{x - Wt}{2\sqrt{Dt}} \right) + e^{Wx/2D} \operatorname{erfc} \left(\frac{x + Wt}{2\sqrt{Dt}} \right) \right] \quad (15)$$

where $U = 2\sqrt{Dk_2}$, $W = 2\sqrt{D(k_2 - \lambda)}$, and $\lambda \approx k_1$. The value of c_0 can be taken as that given by Equation 13 at $x = 0$.

A fully time-dependent solution for $c(x, t)$ under single pulse conditions can also be straightforwardly obtained if the effect of k_1 is approximated by the instantaneous activation at $t = 0$ of a fixed number of molecules $M \sim k_1 t_a$ per cross-sectional area A_{yz} , in the form of a delta function profile at $x = 0$. The standard solution $c(x, t) = M \exp(-x^2/4Dt - k_2 t) / (C_0 A_{yz} \sqrt{4\pi Dt})$ can be equated to c_{sat} and solved for x to obtain the time-evolution of the maximum droplet profile width,

$$x^0(t) = \sqrt{2Dt \left[\ln \left(\frac{w^2}{4\pi c_{sat}^2 Dt} \right) - 2k_2 t \right]} \quad (16)$$

where $w = M/C_0 A_{yz} \sim k_1 t_a$. The extremum of $x^0(t)$ is the maximum possible droplet profile width,

$$x_0^{\max} = \frac{l_0}{2} \sqrt{W(G)[W(G)+2]} \quad (17)$$

where W is the Lambert-W or omega function, $G = w^2/(\pi c_{\text{sat}}^2 l_0^2)$, and $w \sim k_1 t_a$ is the amount of molecules activated per unit of cross-sectional area by the initial pulse. Similar to [Equation 14](#), this expression yields a ratio of oligo to WT profile widths of $\sim 3.5\text{-}4.1$.

The asymptotic behavior of $W(a)$ for $a \rightarrow 0$ is given by its Taylor series as $W(a) = \sum_{j=1}^{\infty} (-j)^{j-1} a^j / j!$. Thus to lowest order $W(a) \sim a$, such that one may roughly approximate $x_0^{\max} \sim k_1 t_a / \sqrt{2\pi c_{\text{sat}}}$ for small $a = k_1 k_2 t_a / D c_{\text{sat}}$. For large a , $W(a)$ is asymptotic to $W(a) = \ln a - \ln(\ln a) + O(1)$, very roughly giving $x_0^{\max} \sim l_0 \ln(k_1 t_a / l_0 \sqrt{\pi c_{\text{sat}}})$. This expression may be compared to [Equation 14](#) for continuous activation. The effects of hard wall boundaries can also be accounted for with standard solution methods.

Model Parameterization

The procedures used to quantify the physical parameters that enter the model of [Equation 11](#) are outlined in this section. A diffusion constant $D = 6.5 \mu\text{m}^2/\text{s}$ was employed based on known values for other intracellular proteins such as GFP, which are typically on the order of $\sim 1\text{--}100 \mu\text{m}^2/\text{s}$. Values of k_1 and k_2 were determined from experiments and the kinetic model as described in the main text. The ratio $c_d/c_{\text{sat}} \sim 25\text{--}100$ was taken to correspond to the measured average intensities of the droplet and background phases, respectively, for a given system. While maintaining this ratio, the particular values for each parameter were scaled such that $c_{0,\text{inact}}/c_{\text{sat}} \sim c_d/c_{0,\text{inact}}$ for the optoFUS system. The supersaturation prefactor S_0 was estimated from typical observed droplet growth rates. Roughly, if droplets of size $R \sim 1 \mu\text{m}$ appear within a time of $t \sim 10 \text{ s}$, then the expression for diffusion-limited growth implies $S_0 \sim R^2/2Dt \sim 0.005$. The heterogeneous nucleation site density n is estimated to correspond to the typical density of droplets, which is on the order of $\sim 1/(2 \mu\text{m})^3$ or $\sim 0.1 \mu\text{m}^{-3}$. The homogeneous nucleation rate prefactor $\chi_0 = (4\pi\gamma_c^2/3k_B T)^{1/2} \sim 2$ is obtained from $k_B T = 4 \times 10^{-21} \text{ J}$, $l_c = 2\gamma v_m/k_B T \sim 3 \text{ nm}$, $\gamma \sim 10^{-5} \text{ J/m}^2$, and $v_m \sim 5 \times 10^{-25} \text{ m}^3$. The latter two values are obtained on general physical grounds; $\gamma \sim k_B T/\xi^2$ and $v_m \sim 4\pi(\xi/2)^3/3$, where $\xi \sim 10 \text{ nm}$ is a typical molecular length scale for proteins. The characteristic homogeneous nucleation time is estimated as $t_c = l_c^2/D c_{\text{eq}}(\infty) v_m \sim 0.002 \text{ s}$, where $c_{\text{eq}}(\infty) \sim 600 \mu\text{m}^{-3}$ is obtained from an estimated molar concentration of $\sim 1 \mu\text{M}$ within the background phase.

Scaling of droplet profile width with physical parameters

To assess the regimes of validity of the equation for the steady-state droplet profile width, systematic variations in the steady-state droplet profile were examined as a function of k_1 , k_2 , D , n , S_0 , c_{sat} , and c_d for a parameterization similar to that of optoFUS ([Figure S6](#)). Many features can be understood from inspection of [Equation 14](#), which is also quoted in the main text. In general, the scalings predicted by [Equation 14](#) are observed in the regimes for which $c(x, t) \rightarrow c_{\text{ss}}(x)$ before significant droplet growth occurs ($1/k_2$ sufficiently small). Deviations grow as the timescales for these two processes become similar and growth begins to diminish profile widths.

- k_1 : A minimum k_1 exists below which $c_{\text{ss}}(0) < c_{\text{sat}}$ and droplets do not appear. This value can be determined from [Equation 14](#) and/or (13). Above this value, $x^{\text{ss}} \sim \ln k_1$ initially, as given by [Equation 14](#), and then plateaus/saturates $\sim l_0$ at large k_1 due to the saturation effect built in via $k_1(1 - c_{\text{tot}})$, also reflected in [Equation 14](#).
- D : For small D , the profile width is limited by spreading and $x^{\text{ss}} \sim \sqrt{D}$ as given by [Equation 14](#). The width then peaks/plateaus at intermediate D as the maximum value of $c(x)$, roughly given by $c_{\text{ss}}(0)$, begins to decrease. Eventually, $c_{\text{ss}}(0)$ approaches and then falls below c_{sat} , reducing x^{ss} back toward 0 at some maximum value of D that can be determined from [Equation 14](#) and/or (13).
- k_2 : A maximum k_2 exists, above which $c_{\text{ss}}(0) < c_{\text{sat}}$ and droplets do not appear. This value can be determined from [Equation 14](#) and/or (13). Below this value, $x^{\text{ss}} \sim 1/\sqrt{k_2}$ initially, as given by [Equation 14](#), since spreading rather than droplet-induced depletion limits the profile width. For sufficiently small k_2 , the timescale for growth becomes $\ll 1/k_2$, and the profile width saturates to a value set by the growth rate alone.
- c_{sat} : A maximum c_{sat} exists, above which $c_{\text{ss}}(0) < c_{\text{sat}}$ and droplets do not appear. This value can be determined from [Equation 14](#) and/or (13). As c_{sat} decreases, $x^{\text{ss}} \sim -\ln c_{\text{sat}}$ initially, as given by [Equation 14](#). The width eventually plateaus at some value $> l_0$ that is determined by the magnitude of c_d and the profile width threshold value ($\theta_d = 0.025$ for the $x_{0.025}^{\text{ss}}$ data shown).
- c_d : Similar to c_{sat} , $x^{\text{ss}} \sim -\ln c_d$ over the range of meaningful c_d values ($c_d \leq c_{\text{sat}}$ is unphysical).
- n : For large n , profile width is limited by the rapid rate of growth and follows $x^{\text{ss}} \sim 1/\sqrt{n}$ (n is roughly analogous to k_2 in the explicit evolution equations). With decreasing n , x^{ss} eventually plateaus $\sim l_0$ as the timescale for growth becomes $\gg 1/k_2$ and steady-state spreading controls profile width.
- S_0 : S_0 is roughly analogous to n and k_2 in the explicit evolution equations, and its scaling behavior can be understood accordingly.

Numerical methods

The mesoscale model evolution equations, [Equation 10](#), were solved using explicit Forward Euler time stepping on a uniform numerical grid with periodic boundary conditions. Laplacian operators were computed in Fourier space via standard FFT methods. A numerical grid spacing $\Delta x = 1$, and time step $\Delta t = 0.005$ were employed, with $\lambda_i = 0.7$, $M_i = 1$, and $k_B T = 1 \times 10^{-8}$.

The coarse-grained model evolution equations, [Equation 11](#), were also solved on a uniform numerical grid using explicit Forward Euler time stepping, with Laplacian operators computed in real space via the second-order central finite difference discretization.

Mirror boundary conditions were employed to model closed finite systems with hard wall boundaries. For heterogeneous nucleation with diffusion-limited growth, [Equation 11](#), was written in rate law form as $dR/dt = DS(t)/R$ or $dV^{1/3}/dt = (4\pi/3)^{2/3}DS(t)/V^{1/3}$ and iterated implicitly in time as

$$V_i^{1/3}(t + \Delta t) = \frac{1}{2} \left[V_i^{1/3}(t) + \sqrt{V_i^{2/3}(t) + \beta DS_i(t)} \right] \quad (18)$$

where $i = [1, 2, \dots, N_x]$ denotes the spatial grid index and $\beta = 4\Delta t(4\pi/3)^{2/3}$. The relation $d\theta_d/dt = n dV/dt$ was then employed to update the droplet volume fraction as $\theta_{d,i}(t + \Delta t) = \theta_{d,i}(t) + n[V_i(t + \Delta t) - V_i(t)]$.

For homogeneous nucleation with diffusion-limited growth, the integral in [Equation 11](#) was discretized and evaluated as follows. The density of droplets nucleated at grid index i over time Δt was computed from the mean-field classical nucleation rate as $J_{hom}\Delta t = (3/4\pi)\Delta t \chi_0^6 S_i^{2/3}(t)[1 + S_i(t)]^{3.55} e^{-1/S_i^2(t)}$ and stored in a two-dimensional array $Q_{i,j}$ of size $N_x \times t_{final}/\Delta t$. The growth of each droplet population within this array was then updated at each Δt according to the diffusion-limited growth law described above for heterogeneous nucleation. The total change in θ_d at i is given by the sum over the growth of each population belonging to the history of slice i ,

$$\theta_{d,i}(t + \Delta t) = \theta_{d,i}(t) + \sum_{j=0}^{t+\Delta t} [Q_{i,j}(t + \Delta t) - Q_{i,j}(t)]. \quad (19)$$

In all simulations, the droplet growth rate was set to zero over any time interval in which the supersaturation $S(t)$ was not positive. Typical numerical parameters used were $\Delta x = 1/2$, $\Delta t \leq 0.01$ (or $\sim 0.01/D$ for large D), and $N_x = 1000$.

Supplemental Figures

Cell

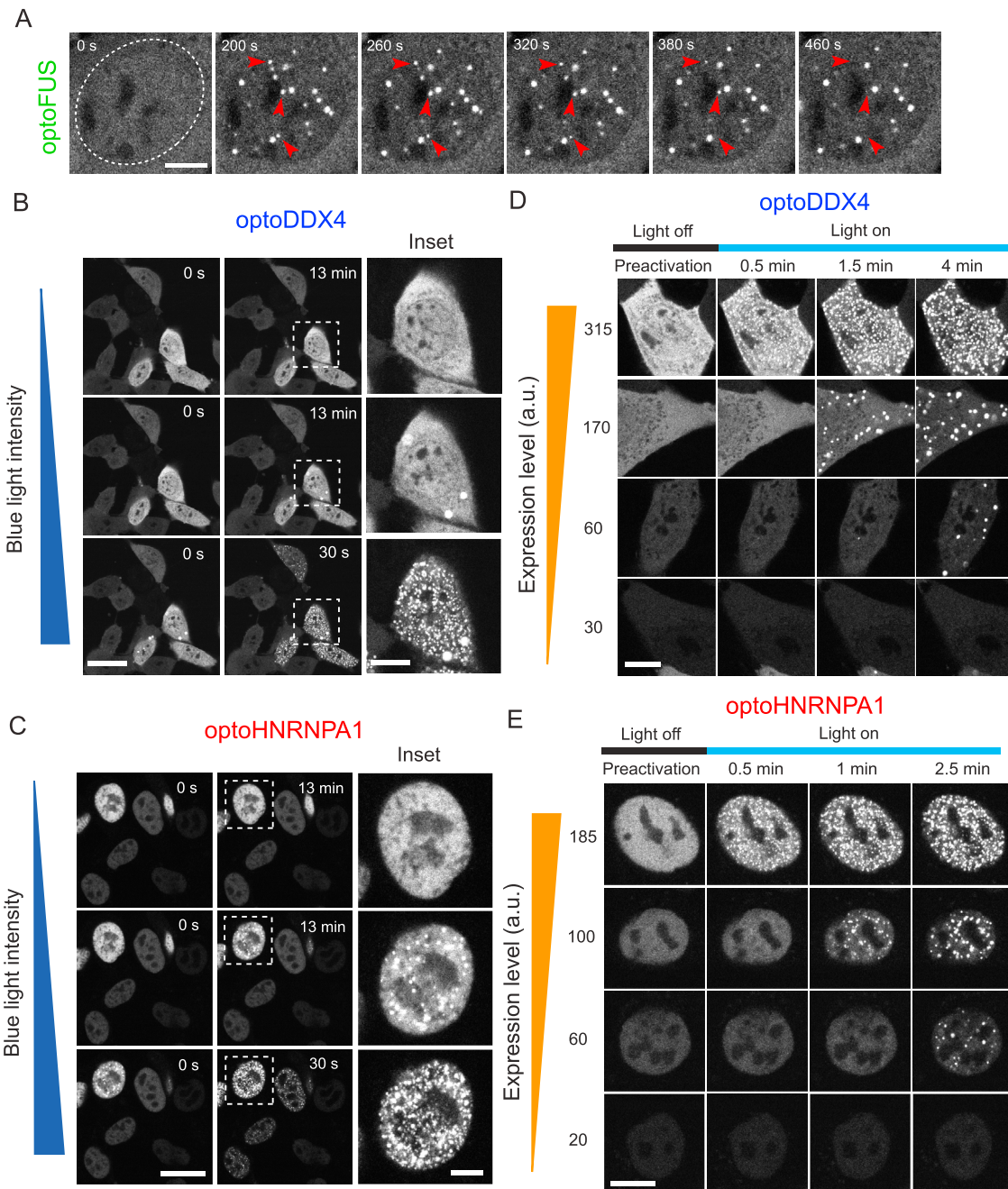


Figure S1. OptoIDR Constructs Show Signatures of Phase Separation, Related to Figures 1 and 2

(A) Assembly dynamics of optoFUS droplets in nucleus is visually consistent with Ostwald ripening. At time 0, blue light activation was initiated. Droplets that fade away over time are highlighted with red arrowheads. A white dashed line indicates nuclear periphery, scale bar = 5 μ m.

(B and C) Blue light intensity dependence of optoDDX4 (B) and optoHNRNPA1 (C) droplet formation. OptoIDR cells were exposed to a sequence of increasing intensity of blue light. (Top) Cells exposed to very weak blue light power showed no droplet formation over 13 min. (Middle) Increasing blue light intensity \sim 2 fold lead to slow nucleation and growth of droplets only in cells with high expression levels. (Bottom) Further increasing activation power resulted in an immediate onset of clustering in many cells. Scale bars, 30 μ m (B, 10 μ m in insets) and 20 μ m (C, 5 μ m in insets).

(D and E) Images of optoDDX4 (D) and optoHNRNPA1 (E) cells with varying expression levels (numeric values on the left, a.u.) exposed to identical activation conditions. Scale bars = 10 μ m.

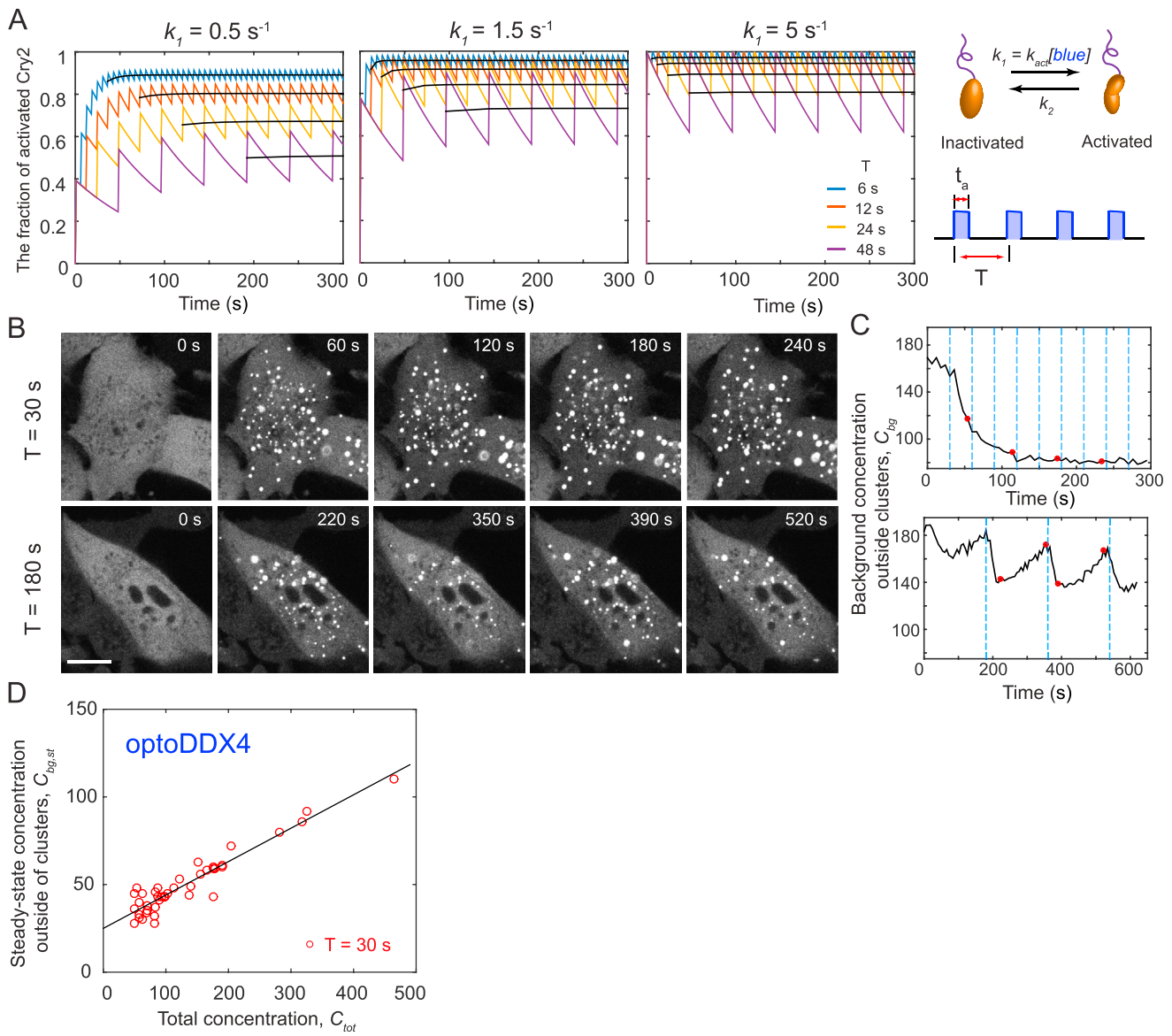


Figure S2. The Cyclic Activation Protocol Used to Quantify C_{sat} and Kinetic Rate Constants for Light-Induced Phase Separation, Related to Figure 3

(A) Example temporal profiles of activated molecule fractions calculated with three different activation rates (see the STAR Methods). Profiles from different activation intervals, T , are plotted with different colors. Black lines are average fractions of activated molecules at steady state, plotted based on the analytic expression. Further increasing the activation rate above $k_1 = 5 \text{ s}^{-1}$ does not change profiles since the activation rate is already high enough to populate the activated state fully during the blue light ON phase. $k_2 = 0.01 \text{ s}^{-1}$ and $t_a = 1 \text{ s}$ are used.

(B) Representative time-lapse images of optoFUS cells for two different activation intervals. Scale bar, $10 \mu\text{m}$.

(C) Temporal evolution of background concentrations outside clusters, C_{bg} , for cells in (B). Red dots denote time points when cell images are taken and blue dashed lines represent time points for blue light activation.

(D) Characterization of C_{sat} for optoDDX4. The cyclic activation protocol identical to one used for optoFUS (Figures 3B and 3C) was applied to measure the saturation concentration of optoDDX4. A solid line is a linear fit to data. The saturation concentration, y-intercept, is 2-fold lower than optoFUS (Figure 3C).

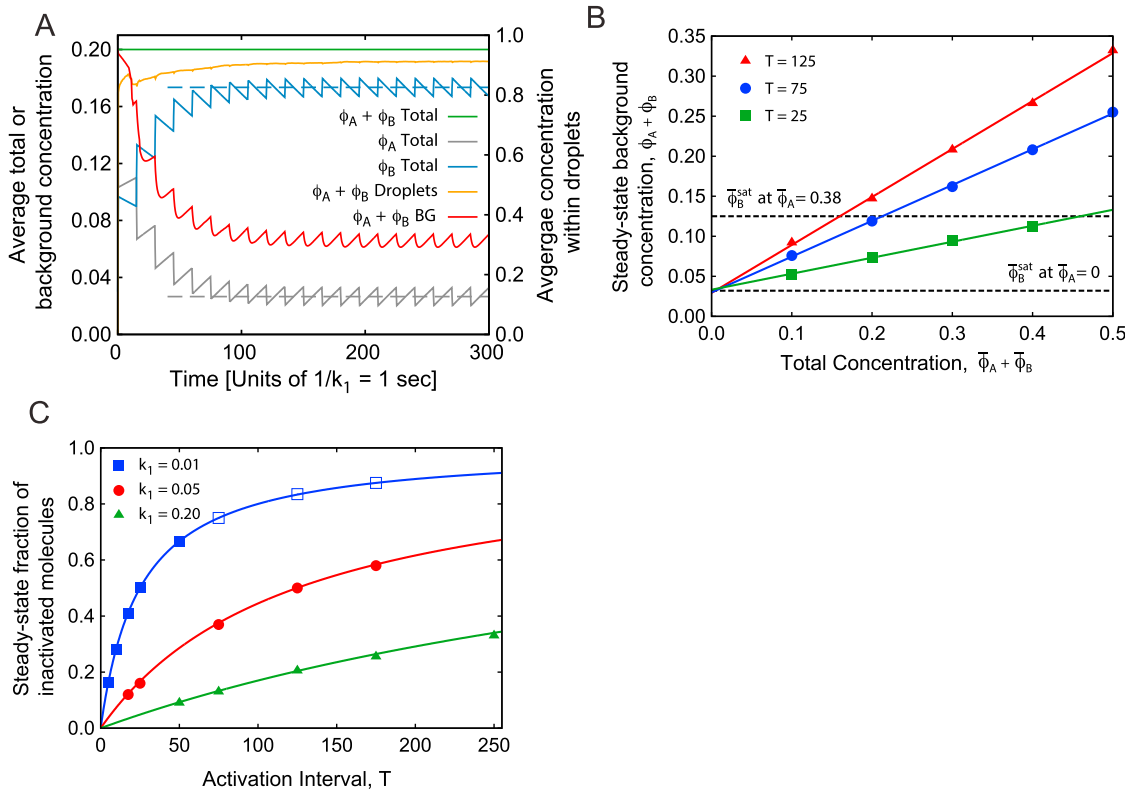


Figure S3. Light-Activated Liquid-Liquid Phase Separation in the Mesoscale Continuum Model Reproduces Experimental Observations, Related to Figure 3

(A) Evolution of various average concentrations for the phase transition pathway highlighted in Figure 3F (red arrow), under a reaction cycling protocol analogous to those employed in the experiments.

(B) Steady-state background concentration versus total concentration for three activation intervals. The linear fits (solid lines) all extrapolate to ~ 0.03 at $\bar{\phi}_A + \bar{\phi}_B = 0$, which corresponds with $\bar{\phi}_B^{\text{sat}}$ at $\bar{\phi}_A = 0$ (lower dashed line). The upper dashed line corresponds to $\bar{\phi}_B^{\text{sat}}$ at $\bar{\phi}_A = 0.38$, the binodal position at the highest expression level considered.

(C) Fraction of inactivated molecules in the steady-state background phase, $\phi_A^{\text{bg,ss}} / (\bar{\phi}_A + \bar{\phi}_B)$, versus activation interval for three forward reaction rates k_1 . Open symbols denote systems in which droplets do not form. Solid lines are $1 - F_{\text{act,sv,av}}$ predicted by the kinetic model (see Equation 8 in the STAR Methods), with no free parameters. In all simulations, the initial condition was a homogeneous liquid with $\bar{\phi}_B = 0.03$, and the ON portion of the activation interval was fixed at $2.5t$. Droplet nucleation between the binodal and spinodal boundaries was facilitated by a stochastic droplet seeding algorithm based on classical nucleation theory in the mean-field limit.

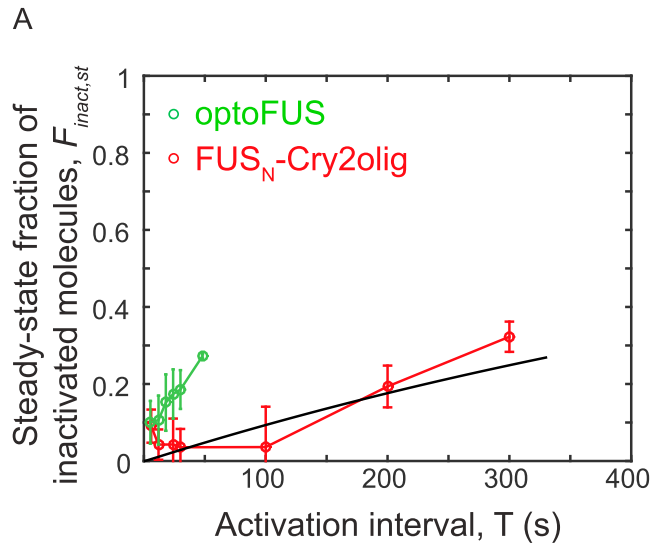


Figure S4. Slower Inactivation Kinetics of FUS_N -Cry2olig Compared to optoFUS, Related to Figure 4

The cyclic activation protocol identical to one used for optoFUS (Figure 3D) was applied to FUS_N -Cry2olig cells to characterize inactivation kinetics. Fractions of inactivated molecules for various activation intervals are plotted. A blue laser intensity of $0.3 \mu\text{W}$ is used and data for optoFUS (a replica of Figure 3D for the same blue light power) are shown for comparison. A solid line is a fit using the kinetic model with a fixed k_1 of measured value for optoFUS, yielding $k_2 = 0.002 \pm 0.0008 \text{ s}^{-1}$. Error bars are SD.

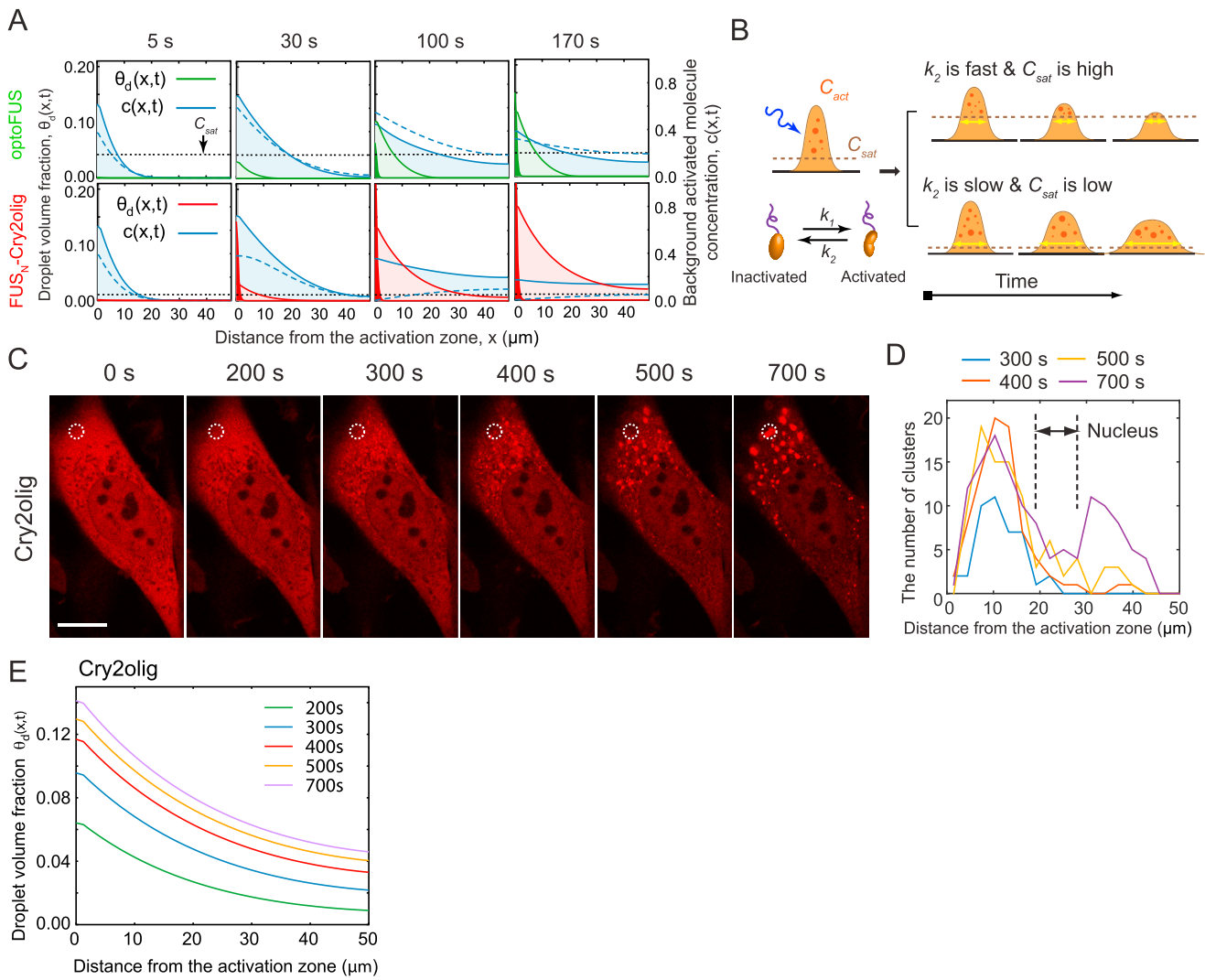


Figure S5. Physical Parameters Governing Localized Phase Separation, Related to Figure 5

(A) Temporal evolution of background activated molecule concentration, $c(x,t)$, and cluster volume fraction, $\theta_d(x,t)$, for continuous localized activation of optoFUS (top) and FUS_N-Cry2olig (bottom), analogous to experiments in Figures 5A and 5F, calculated using the coarse grained phase transition model. Solid and dashed lines indicate profiles for heterogeneous nucleation and homogeneous nucleation, respectively. Cluster volume fractions simulated for homogeneous nucleation are highly confined near the activation zone. The cluster volume fraction data for heterogeneous nucleation are replicas of Figures 5B and 5G. Horizontal dotted lines denote c_{sat} . All parameters (listed in Tables S1 and S2) except two, k_2 and c_{sat} , are shared for both calculations.

(B) Schematic diagram illustrating the broadening effects of slower inactivation kinetics and lower C_{sat} on the localized phase transition.

(C) Time-lapse images of Cry2olig for localized activation. The activation condition same as those for optoFUS and FUS_N-Cry2olig in Figures 5A and 5F is used. White dotted lines denote the activated zone. Scale bar, 10 μm .

(D) Temporal evolution of cluster number distribution over distances away from the activation zone for clusters in (C). Concomitant appearance of clusters on one side of cell, apparently blocked by nucleus, is followed by cluster formation in the other side of cell at a later time. Note that cluster appearance for Cry2olig is much slower than for optoFUS and FUS_N-Cry2olig.

(E) Temporal evolution of droplet volume fraction distribution calculated from the coarse-grained phase transition model for localized activation of Cry2olig. Parameters used are identical to those for FUS_N-Cry2olig in (A) except $S_0 = 0.0005$ rather than 0.005 (all other parameters are listed in Table S1).

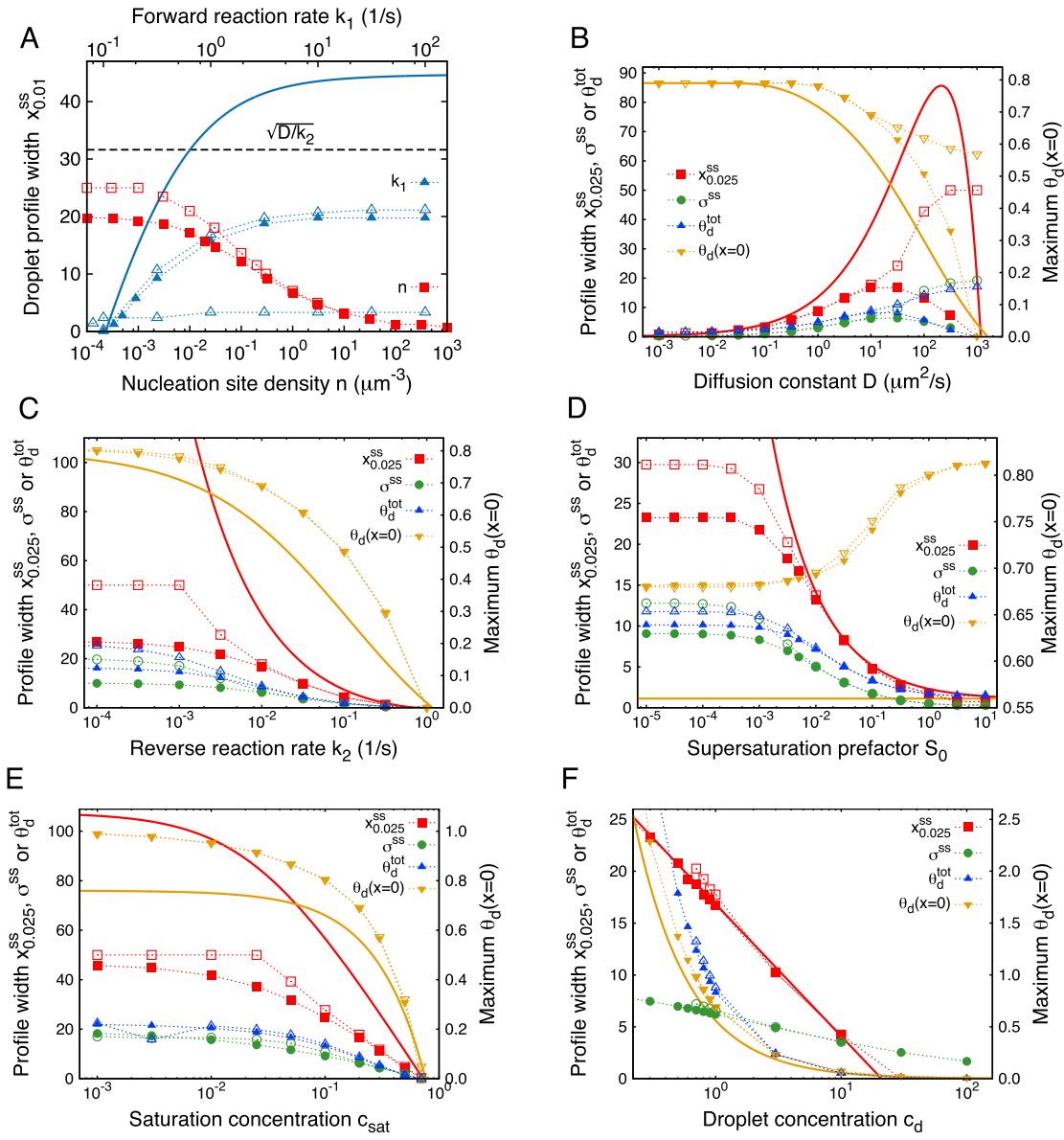


Figure S6. Measures of the Steady-State Droplet Volume Fraction Profile $\theta_d(x)$ from the Coarse-Grained Phase Transition Model with Heterogeneous Nucleation, Related to Figure 5

(A–F) Parameter-sweeps have been performed for continuous localized activation shown in Figure S5A using the coarse-grained phase transition model. Here, explicit inactivation kinetics within the droplet phase is neglected ($d\theta_d/dt = d\theta_d^{\text{g}}/dt$) for simplicity. Fixed parameters are those used for optoFUS, except $D = 10$, $c_d = 1$ and $n = 0.2$. $x_{0.025}^{\text{ss}}$ is the position at which $\theta_d(x) = 0.025$, σ^{ss} is the standard deviation of $\theta_d(x)$, θ_d^{tot} is the total amount of droplet phase in the system, and $\theta_d(x = 0)$ is the maximum θ_d in steady-state, at the activation zone. Results from simulations with a system size, L_x , sufficiently large to be effectively infinite are shown with closed symbols, and simulations with $L_x = 50 \mu\text{m}$ are shown with open symbols. Solid lines in (A)–(D) are analytical results from Equation 14, in the limit $c(x,t) \rightarrow c_{\text{ss}}(x)$ and $\theta_d(x) \rightarrow (c_{\text{ss}}(x) - c_{\text{sat}})/c_d$. Solid lines in (E)–(F) are qualitative fits to the general functional forms expected based on Equation 14. See the STAR Methods for further detailed explanation.

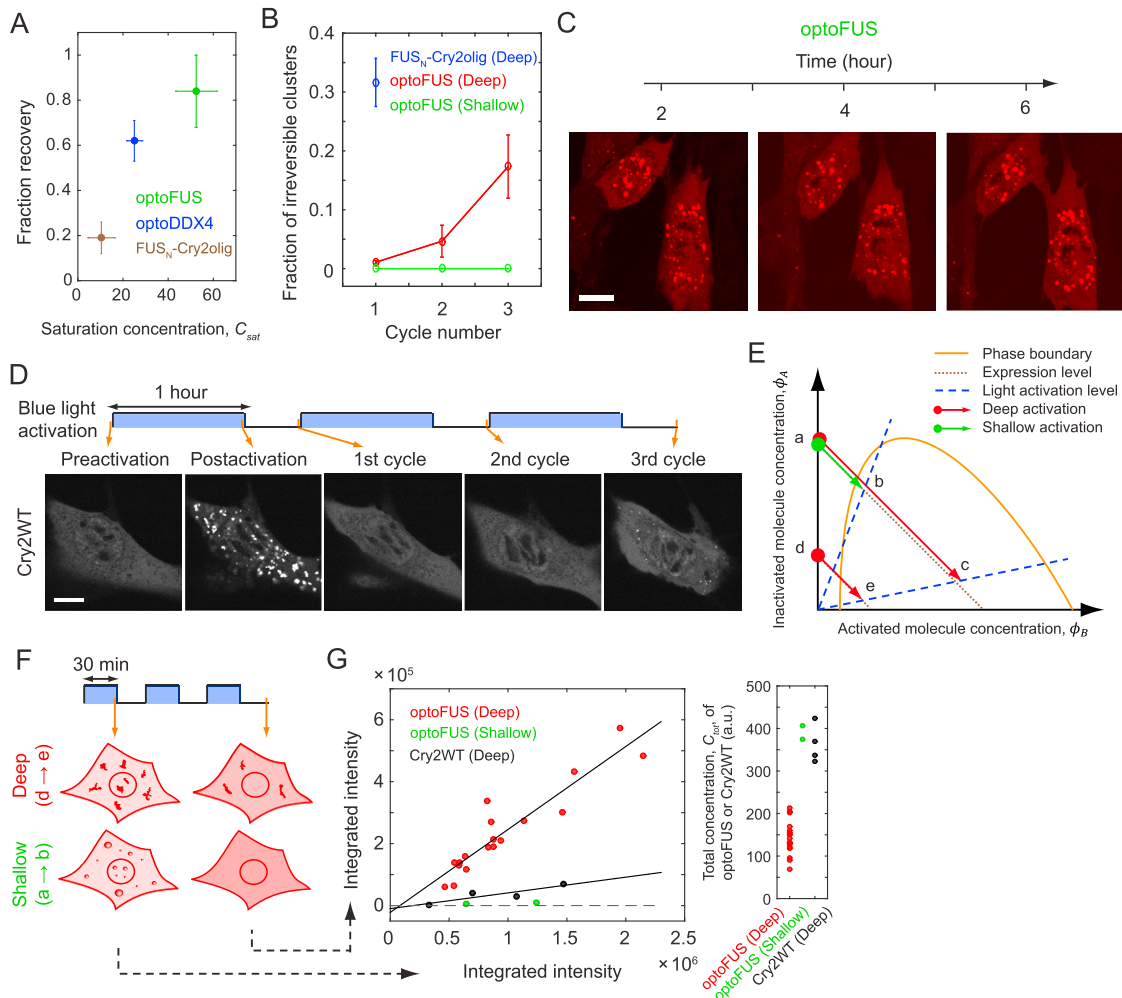


Figure S7. The Gel State Promotes Formation of Irreversible Aggregates, Related to Figure 6

- (A) Saturation concentration, C_{sat} , versus fraction recovery in FRAP measurements. The saturation concentration of each construct is from measurements with cyclic activation protocols (Figures 3C, 4C, and S2D). Values for fraction recovery are from FRAP data (Figure 6A). Error bars represent 95% confidence intervals of fits (C_{sat}) and SDs (fraction recovery in FRAP), respectively.
- (B) Fractions of irreversible aggregates over each assembly/disassembly cycle for optoFUS and FUS_N-Cry2olig. During assembly, cells were activated for 10 min with corresponding activation conditions. For FUS_N-Cry2olig, single cycle of assembly and disassembly is enough to produce irreversible aggregates. Data show mean \pm SD ($n = 3$ for each condition).
- (C) Fluorescence images of optoFUS cells with irreversible aggregates in the absence of blue light. Cells first underwent 5 cycles of “deep” assembly/disassembly, under the identical condition as used in Figure 6G. Images were taken at the indicated time points (the end of fifth assembly is time 0). Scale bar = 10 μ m.
- (D) Cry2WT (no FUS fusion) forms irreversible aggregates after long activation cycles. For assembly cycle, a Cry2WT cell with similar expression level as those in Figure 6G was activated for 1 hr with identical “deep” blue light condition.
- (E) Schematic describing different experimental conditions used in Figures 6, S7F, and S7G. Experiments in Figure 6 were performed for cells with relatively high expressions. Light induced phase transition on these cells leads to transitions in the phase diagram either from state a to b (shallow) or from a to c (deep). The total amount of phase separated materials for deep activation is higher than for shallow activation. Deep activation on the low expression cells (a transition from state d to e in the phase diagram) leads to similar amount of cluster formation as the shallow activation in high expression cells.
- (F) Schematic illustrating activation procedures and measured parameters used in (G). To induce observable amount of irreversible aggregates in weakly expressing cells, the cluster assembly time is extended to 30 min. Integrated intensities of clusters at the end of the first assembly and the third disassembly are plotted in (G).
- (G) (Left) Even when the total amount of phase separated gels is comparable or smaller than that of liquid droplets, gels robustly form irreversible aggregates. As a control, data from Cry2WT cells that undergo identical “deep” activation conditions are shown. Two black solid lines are linear fits to data (optoFUS “deep” and Cry2WT “deep”) and a dashed horizontal line denotes zero. (Right) Total intracellular concentrations of the optoFUS or Cry2WT constructs used for this comparison.